Numerical implementation of a non-local GTN model for explicit FE simulation of ductile damage and fracture

Sondre Bergo [a,b,*], David Morin [a,b] and Odd Sture Hopperstad [a,b]

[a] Structural Impact Laboratory (SIMLab), Department of Structural Engineering, Norwegian University of Science and Technology (NTNU), NO-7491 Trondheim, Norway

[b] Centre for Advanced Structural Analysis (CASA), NTNU, NO-7491 Trondheim, Norway

Abstract

In this study, we follow the work of Tvergaard & Needleman (1995), Tvergaard & Needleman (1997) and Needleman & Tvergaard (1998) and present the numerical implementation and some initial applications of a non-local Gurson-Tvergaard-Needleman (GTN) model for explicit finite element (FE) analysis. The delocalization relates to the damage mechanism and is incorporated in terms of an integral condition on the rate of change of the porosity. In order to demonstrate the mesh independence during all stages of ductile damage and fracture, several material test specimens have been simulated until full fracture using different mesh sizes. For comparison purposes, results are also obtained for the corresponding local GTN model in all cases. The effect of the material characteristic length on the ductile damage and fracture behavior and on the mesh sensitivity of the results is discussed. It is shown that simulation results obtained in all stages of the ductile fracture process, including void growth, fracture initiation by coalescence and crack propagation all the way to a fully fractured specimen, are mesh independent from a certain ratio of mesh size relative to the material characteristic

length, provided the non-local integral is evaluated on the current configuration. This ratio is unique for each individual specimen simulated as it depends on the spatial gradients of the porosity and the material parameters adopted for the problem at hand. It is shown that excessive averaging at large deformations occurs if the non-local integral is evaluated on the reference configuration, i.e., without updating the element interaction matrix resulting from the discretization of the non-local integral.

Keywords: non-local, strain localization, ductile crack initiation and propagation, Gurson-Tvergaard-Needleman model

*Corresponding author: Sondre Bergo (sondre.bergo@ntnu.no)

Declaration of competing interests: The authors declare that they have no competing interests.

1 Introduction

The study of crack initiation and propagation is important for the assessment of the integrity of engineering metal structures. Unfortunately, major challenges are faced when applying numerical predictive tools for the simulation of the ductile fracture process. In ductile fracture, which is the most dominant failure mode in metals and alloys at room temperature and above, the main damage mechanism is nucleation, growth and coalescence of microscopic voids at inclusions and second-phase particles. A large number of predictive computational models have been proposed in the literature to

provide a physical description of these mechanisms, see e.g. the reviews by Benzerga & Leblond (2010) and Pineau et al. (2016) and references therein for in-depth descriptions and discussions of these models.

The perhaps most popular ductile damage model was proposed by Gurson (1977), where the damage mechanism is regarded through a constitutive variable representing the porosity (or void volume fraction), denoted f. The evolution of the porosity predicted by the Gurson model follows as a direct consequence of the requirement of mass conservation of a porous rigid plastic material assuming plastic incompressibility. Accordingly, material degradation is in a general sense characterized by the presence and evolution of microvoids. The fact that the Gurson model predicts material degradation implies that it is classified as a "coupled" damage model, i.e., the "damage" parameter (in form of the porosity f) is involved in the constitutive equations and decreases the stress-carrying capacity of the material as it evolves, which eventually results in strain softening. The original Gurson model was only able to predict the void growth phase. Chu & Needleman (1980) proposed void nucleation models controlled by the local stress or plastic strain. The original Gurson model was subsequently extended by Tvergaard and Needleman, first by the introduction of the q_i parameters (Tvergaard, 1981, 1982) and then by modifying the yield condition to incorporate coalescence of microvoids (Needleman & Tvergaard, 1984; Tvergaard & Needleman, 1984), in order to be in better agreement with unit cell simulations and experimental measurements. The model with these modifications included is denoted the Gurson-Tvergaard-Needleman (GTN) model.

The GTN model has since been the target of several extensions, some more universally approved than others. An important contribution is the Lode parameter dependent term in the void evolution proposed by Nahshon & Hutchinson (2008), to resolve the limitation

of the GTN model to correctly predict failure under low stress triaxiality. A similar extension to the GTN model that incorporates Lode parameter dependency motivated by unit cell analyses was proposed by Dæhli et al. (2017). Other notable extensions incorporate different characteristics of the voids, like void shape, orientation and rotation, see e.g. the works of Gologanu et al. (1993), Pardoen & Hutchinson (2000), Benzerga et al. (2004) and Keralavarma & Benzerga (2010).

Coupled ductile damage models such as the GTN model have been, and are still, widely used for predicting the load-deformation behavior and the fracture resistance of structural components. The GTN model is perhaps the most popular model describing ductile damage by microvoid evolution and has been applied to most scenarios involving ductile failure. A few selected recent applications of the GTN model found in the literature involve ductile fracture predictions (see e.g. Teng et al. (2017), Gholipour et al. (2019), Bahrami Ghalehjoogh & Hoseini (2018), and Jiang et al. (2016)), damage evaluation for hot forming processes (Imran & Bambach, 2018), and simulation of ductile crack growth (e.g. Oh et al. (2017) and Qiang & Wang (2019)).

Constitutive models in which the evolution of material damage at a point is a function of the stress and strain fields at the same point, i.e., the material law is independent of the surrounding material points, are called local models. Most numerical studies of failure in ductile materials have been based on such local constitutive models, which do not incorporate a material length scale. The GTN model and its extensions mentioned above are examples of local constitutive models.

The predicted initiation and propagation of a crack by a coupled model always takes place in regions where the damage localize. Local constitutive models with coupled damage are well known to exhibit an inherent mesh sensitivity, since the softening material behavior

will give localized damage in regions as narrow as possible within the mesh resolution. This is a result of spurious mesh dependence of the FE solution due to the loss of ellipticity of the equilibrium equations in the softening regime. The dissipated energy converges to zero for infinitesimal element size, which contradicts the physical observation that both the localization width and the energy dissipated by fracture are material properties (see e.g. Needleman (1988)). As a result, the finite element mesh size becomes an additional model parameter, which influences all other model parameters. Thus, it is generally not possible to use the same damage parameters in FE simulations of the same problem with different element sizes.

Despite the significant advances in the development of coupled ductile damage models, such as the GTN model, most of the proposed extensions have been conceived under the hypothesis of a local continuum, i.e., that the material behavior is independent of the surrounding material points. Some contributions in the literature have tried to tackle the issue of localization and the resulting mesh sensitivity of local strain-softening damage models, by aiming to provide mesh-insensitive constitutive models. In 1988, the first non-local plasticity model intended to serve as a localization limiter was proposed by Bazant & Lin (1988). In non-local material models, the softening state of a material point does not depend on the deformation history of this point only. Rather, a non-local state variable is introduced as a weighted average of the local states of the surrounding points.

Non-local modifications that can be applied for strain-softening damage models may be divided into two main categories, namely integral and gradient types. Considering specifically non-local extensions of the GTN model, examples of integral-type numerical implementations can be found in e.g. Leblond et al. (1994), Tvergaard & Needleman (1995), Enakoutsa et al. (2007), and Andrade et al. (2014). Examples of gradient-type

numerical implementations of the non-local GTN model can be found in e.g. Ramaswamy & Aravas (1998), Reusch et al. (2003), Hakansson et al. (2006), Linse et al. (2012), Hütter et al. (2013), and Zybell et al. (2014). What is common between the different types of numerical implementation of the GTN model, is that all non-local modifications aim for a minimization of mesh dependence through direct or indirect regularization of the damage variable, namely the porosity f.

As mentioned by Nguyen et al. (2014), the interest generated by the non-local description of ductile crack propagation is only relatively recent (see e.g. the work by Engelen et al. (2003)) and the attention is mainly devoted to provide physically valid (e.g. Andrade et al. (2011) and Peerlings et al. (2012)) and numerically efficient models (e.g. Belnoue et al. (2010) and Seabra et al. (2013)). Although the interest is rather recent, some successful applications of the non-local description of ductile crack initiation and propagation have been reported in the literature. As an example, Linse et al. (2012) extended the GTN model using an implicit gradient formulation and were able to model mesh-independent crack initiation. They chose to modify the GTN model by replacing the dilatational plastic strain rate by its non-local spatial average in the evolution equation of the existing voids, all other equations were left unaltered.

Hütter et al. (2013) used a slightly modified version of the non-local GTN model proposed by Linse et al. (2012), and pointed out problems in handling full material failure. Problems arise if the evolution of the localization zone is to be simulated up to the complete loss of stress-carrying capacity. Fully failed Gauss points in the finite element formulation still contribute in an implicit framework, as pointed out by Geers et al. (1998), Simone et al. (2003) and Peerlings et al. (2002). In many studies (e.g. Samal et al. (2008), Seidenfuss et al. (2011), and Reusch et al. (2008)), the local values are fixed at the

moment of failure, although the fully failed zone still has to be solved for equilibrium. Linse et al. (2012) tried to introduce a new surface with trivial Neumann boundary conditions where failure occurred, but faced severe numerical problems. Hütter et al. (2013) expanded on the work by Linse et al. (2012) by introducing a Dirichlet boundary condition for the fully failed material, and were as a result able to model larger amounts of crack propagation than in comparable preceding studies.

The objective of the work herein is to follow up on the assessment of delocalization methods for coupled damage models, focusing on crack initiation, propagation and full fracture. Even though the idea of introducing a material length scale into the constitutive equations was first mentioned more than 30 years ago, the development, application and assessment of non-local GTN models is still an active field of research. We build further upon the non-local model proposed by Tvergaard & Needleman (1995) which is of the integral type, regularizing the rate of change of the porosity. The explicit FE method is chosen in order to avoid the convergence problems at complete loss of stress-carrying capacity discussed by Hütter et al. (2013) amongst others. The integral type non-local formulation further has the advantage of being completely defined on the material level, which makes this approach particularly suitable for explicit FE methods. Many of the advantages of the constitutive modelling at finite strains within the local framework can be extended in a straight-forward manner to the non-local case, retaining the applicability of the GTN model.

Our implementation of the non-local GTN model differs from previous work in the literature in the following:

1. A new form of a staggered update of the non-local porosity relevant for explicit FE analyses is proposed and validated.

2. The non-local porosity is updated also for elements in the elastic domain, in order to avoid a decreasing size of the plastic zone as the mesh is refined. The elastic elements are checked for yielding in the subsequent time step, and if plasticity occurs, consistency is enforced through the return mapping algorithm.
3. The element interaction matrix is also updated in each time step based on the current configuration, in contrast to a fixed interaction matrix throughout the simulation most commonly applied in the literature (see e.g. Leblond et al. (1994), Tvergaard & Needleman (1995), Tvergaard & Needleman (1997), Needleman & Tvergaard (1998), Enakoutsa (2014) and Enakoutsa et al. (2007)).

In the present study, our proposed non-local GTN model is applied to ductile fracture of typical material test specimens, and emphasis is put on the predicted global response and the evolution of the porosity and equivalent plastic strain fields in the vicinity of the propagating crack.

2 Constitutive modeling

2.1 Local GTN model

The non-local extension applied here consists of minor, but important, changes to the local GTN damage model, and for completeness, the main equations of the local GTN model are summarized in the following.

The GTN model is formulated here using a corotational stress formulation with the assumption of small elastic strains. Linear hypoelasticity is adopted to describe the elastic behavior of the isotropic material, which is defined by Young's modulus E and Poisson's ratio ν. The yield condition of the GTN model is defined as:

$$\Phi = \left(\frac{\sigma_{\mathrm{eq}}}{\sigma_{\mathrm{M}}}\right)^2 + 2f^* q_1 \cosh\left(\frac{q_2}{2}\frac{\mathrm{tr}\boldsymbol{\sigma}}{\sigma_{\mathrm{M}}}\right) - \left(1 + q_3 f^{*2}\right) = 0 \tag{1}$$

where $\sigma_{\mathrm{eq}} = \sqrt{3\boldsymbol{\sigma}' : \boldsymbol{\sigma}'/2}$ is the von Mises equivalent stress, $\boldsymbol{\sigma}'$ being the deviatoric part of the Cauchy stress tensor $\boldsymbol{\sigma}$, f^* is the effective porosity, and q_1, q_2, q_3 are the Tvergaard parameters (Tvergaard, 1981, 1982). Furthermore, σ_{M} is the flow stress of the matrix material, defined by the extended Voce rule $\sigma_{\mathrm{M}} = \sigma_0 + \sum_{i=1}^{3} Q_i(1 - \exp(-C_i p))$, where σ_0 is the initial yield stress, Q_i and C_i are hardening parameters, and p is the equivalent plastic strain. We use, here, the typical convention that $q_3 \equiv q_1^2$.

The modified porosity $f^*(f)$ accounts for the effects of rapid void coalescence at failure and is taken to have the form proposed by Tvergaard & Needleman (1984):

$$f^*(f) = \begin{cases} f, & f < f_{\mathrm{C}} \\ f_{\mathrm{C}} + \dfrac{f_{\mathrm{U}}^* - f_{\mathrm{C}}}{f_{\mathrm{F}} - f_{\mathrm{C}}}(f - f_{\mathrm{C}}), & f \geq f_{\mathrm{C}} \end{cases} \tag{2}$$

where f_{C} is the critical porosity. When the porosity reaches this critical value, void coalescence occurs and the void growth accelerates until f_{F} is reached, which is the total porosity at macroscopic failure. Finally, $f_{\mathrm{U}}^* = f^*(f_{\mathrm{F}})$ is the effective void volume at macroscopic failure, which equals $f_{\mathrm{U}}^* = 1/q_1$ for $q_3 \equiv q_1^2$.

As for metal plasticity, the associated flow rule is adopted to define the plastic rate-of-deformation tensor $\mathbf{D}^{\mathrm{p}}$, which can be written as

$$\mathbf{D}^{\mathrm{p}} = \dot{\lambda}\,\frac{\partial \Phi}{\partial \boldsymbol{\sigma}} \tag{3}$$

where $\dot{\lambda}$ is the plastic multiplier. The flow stress of the matrix material σ_{M} in the yield condition is a function of the equivalent plastic strain p (through the extended Voce rule), whose evolution equation reads

$$\dot{p} = \frac{\boldsymbol{\sigma}: \mathbf{D}^{\mathrm{p}}}{(1-f)\sigma_{\mathrm{M}}} \tag{4}$$

The porosity f evolves due to growth of existing voids, $\dot{f}_{\mathrm{G}}$, nucleation of additional voids, $\dot{f}_{\mathrm{N}}$, and void softening in shear, $\dot{f}_{\mathrm{S}}$ (introduced by Nahshon & Hutchinson (2008)):

$$\dot{f} = \dot{f}_{\mathrm{G}} + \dot{f}_{\mathrm{N}} + \dot{f}_{\mathrm{S}} \tag{5}$$

where

$$\dot{f}_{\mathrm{G}} = (1-f)\mathrm{tr}\mathbf{D}^{\mathrm{p}} \tag{6}$$

$$\dot{f}_{\mathrm{N}} = A_N\, \dot{p} \tag{7}$$

$$\dot{f}_{\mathrm{S}} = k_{\mathrm{S}} f \left(1 - \left[\frac{27 J_3}{2\sigma_{\mathrm{eq}}^3}\right]^2\right) \frac{\boldsymbol{\sigma}': \mathbf{D}^{\mathrm{p}}}{\sigma_{\mathrm{eq}}} \tag{8}$$

In these equations, A_N is the constant nucleation rate, $J_3 = \det(\boldsymbol{\sigma}')$ is the third deviatoric stress invariant, and k_{S} is a parameter governing the void softening in shear. When void softening in shear is introduced, f should be considered as an effective porosity or rather as a damage variable (Nahshon & Hutchinson, 2008), but, for simplicity, it will still be denoted porosity in this study.

2.2 Non-local GTN model

The establishment of a non-local constitutive model starts with the definition of the non-local quantity. Several variables may be formulated in a non-local way in order to regularize the strain-softening behavior present in coupled damage models. For the GTN model, the softening mechanism is introduced through the local porosity f, and it is reasonable to regularize this variable in order to avoid excessive and unlimited localization.

The non-local GTN model is obtained by substituting f by the non-local porosity $\bar{f}$ in all equations where it appears in Section 2.1. Adopting the non-local formulation of integral type, we define the non-local porosity $\bar{f}$ in a material point currently at $\boldsymbol{x}$ by the non-local evolution equation:

$$\dot{\bar{f}}(\boldsymbol{x}) = \frac{1}{W(\boldsymbol{x})} \int_V w(\boldsymbol{x} - \boldsymbol{y})\, \dot{f}(\boldsymbol{y}) dV \tag{9}$$

where V is the current volume, while $\boldsymbol{x}$ and $\boldsymbol{y}$ are position vectors. The local rate of change of the porosity $\dot{f}$ is still calculated by means of Equations *(5)*-*(8)*, but with f replaced by $\bar{f}$. The weight function w is defined as proposed by Tvergaard & Needleman (1995):

$$w(z) = \left[\frac{1}{1 + \left(\frac{z}{L}\right)^{p_\mathrm{w}}} \right]^{q_\mathrm{w}} \tag{10}$$

where $z = \sqrt{\boldsymbol{z} \cdot \boldsymbol{z}}$ with $\boldsymbol{z} = \boldsymbol{x} - \boldsymbol{y}$ is the distance between the neighboring material points in the current configuration, $L > 0$ is the material characteristic length, $p_\mathrm{w} = 8$ and $q_\mathrm{w} = 2$ are constants defining the shape of the weight function. This results in a weight close to unity if $z < L$, and a weight close to zero if $z > L$, with a narrow transition region. The function $W(\boldsymbol{x})$ is defined as:

$$W(\boldsymbol{x}) = \int_V w(\boldsymbol{x} - \boldsymbol{y}) dV \tag{11}$$

The local formulation corresponds to the limit $L \to 0$. With $L > 0$, $\dot{\bar{f}} \equiv \dot{f}$ if and only if $\dot{f}$ is spatially uniform. Hence, non-locality is associated with spatial gradients in $\dot{\bar{f}}$.

2.3 Numerical Considerations

We have implemented the non-local GTN model as a user-material subroutine for the explicit solver of the commercial FE code Abaqus adapting the return mapping algorithm proposed by Aravas (1987). In a local explicit FE analysis, the stress state is computed at each Gauss point separately, and only the strain increment and the values of the internal variables at the previous time step are needed in the stress update (assuming proper rotation of the stress tensor due to spin). However, when using a non-local constitutive model, the spatial location of the material point plays a major role in the stress update. In practice, this means that the non-local averaging integral needs to be spatially discretized, which leads to an element interaction matrix giving the contribution from neighboring elements when updating the non-local variable. In the present implementation of the non-local GTN model, the element interaction matrix is updated in each time step based on the current geometry.

In explicit FE analyses in which the strain increments are assumed to be very small, simplifications are justifiable in the incremental update of the non-local variable. Tvergaard & Needleman (1995) introduced a scaling parameter $\kappa_n = \Delta\bar{f}_n/\Delta f_n$, and defined the incremental update of the non-local porosity as

$$\Delta\bar{f}_{n+1} \approx \frac{\Delta\bar{f}_n}{\Delta f_n}\Delta f_{n+1} = \kappa_n \Delta f_{n+1} \tag{12}$$

where the index indicates the time step, and $\Delta(\blacksquare)$ is the increment in the quantity $(\blacksquare)$ during the actual time step. The problem with this update is that even though κ_n is fixed from the previous time increment, the increment of the local porosity Δf_{n+1} is unconstrained and calculated to obtain local consistency in the return mapping algorithm, which necessarily results in slightly different non-local porosity fields with

mesh refinement. The result is that although the obtained global response certainly is regularized, it is not necessarily mesh independent. Tvergaard & Needleman (1995) applied the non-local GTN model in simulations of a compact tension specimen in their following work (Needleman & Tvergaard, 1998), and reported problems in getting mesh-independent predictions of the crack initiation and subsequent crack propagation.

As an alternative, we thus propose a staggered update of the non-local porosity relevant for explicit FE analyses, namely:

$$\bar{f}_{n+1} = \bar{f}_n + \Delta\bar{f}_n, \tag{13}$$

where $\Delta\bar{f}_n$ is calculated according to Equations *(9)*–(11) using the local increments Δf_n and the geometry of the previous timestep. It follows that $\bar{f}_{n+1}$ is treated like a constant in the stress-update algorithm. It will be shown in the subsequent examples that this update scheme provides mesh-independent solutions for crack initiation and propagation. To obtain mesh independence, the non-local porosity has to be updated also for elements in the elastic domain. The elastic elements are checked for yielding in the subsequent time step, and if plasticity occurs, consistency is enforced through the return mapping algorithm. Crack propagation is described by element erosion, and deleted elements do not contribute to the non-local integral.

Whereas the element interaction matrix is here updated in each time step based on the current configuration, several studies have applied a fixed element interaction matrix calculated once over the initial configuration. Henceforth, we will denote the latter for a *fixed* nonlocal method and the former for an *updated* nonlocal method. As we will discuss in the last numerical example, the use of a fixed element interaction matrix is a probable reason for problems with excessive regularization reported in the literature, see e.g.

Leblond et al. (1994), Tvergaard & Needleman (1995), Tvergaard & Needleman (1997), Needleman & Tvergaard (1998), Enakoutsa (2014) and Enakoutsa et al. (2007). To reduce the storage need and computation time, only neighboring elements within a cut-off radius of $1.3L$ from an element are included in the element interaction matrix, as the contributions from elements outside this radius are deemed negligible. While the contributions from each of the neighboring elements are updated at each time step, the list of neighboring elements is updated approximately 50 times throughout a simulation. It was found that increasing the cut-off radius further had basically no effect (differences of 1e-3 to 1e-4 in f) on the obtained results and the same holds for decreasing the interval between the updates of the neighbor list. We note that these numerical artefacts to reduce the storage need and computation time can be rather problem dependent.

3 Numerical Results

The explicit solver of the commercial FE code Abaqus is applied in the numerical simulations in order to describe the damage evolution and crack propagation all the way to a fully fractured specimen. When running quasi-static simulations using an explicit FE code, it is very important to keep the kinetic energy sufficiently low. In our simulations, all specimens were assigned a scaled density resulting in the same amount of (negligible) kinetic energy across different mesh resolutions. In the following examples, results from simulations of several material tests obtained with the local and non-local GTN models described above are compared. In the last example (i.e., the 3D simulation of a tensile test on a cylindrical specimen), we also demonstrate the differences that occur by evaluating

the non-local integral on the reference configuration, using a constant element interaction matrix calculated once at the beginning of the simulation, or on the current configuration. All data presented are extracted from a fully fractured specimen, and in all but the last example shown on the initial configuration for simplicity. Except in the first numerical examples, the hardening parameters are representative for an X65 steel alloy, while the fracture parameters are selected for illustrative purposes.

3.1 Shear banding in a perfectly plastic material

In the first example, the formation of a shear band in a plane-strain tension specimen with a geometrical imperfection is considered. The specimen geometry, taken from Seupel et al. (2018), is given in Figure 1, and the material parameters are compiled in Table 1. The material parameters were chosen in order to trigger an inclined shear band. Perfect plasticity (i.e., a non-hardening material) is assumed to more readily develop the shear band, and it will be illustrated that perfect plasticity results in slower convergence when the porosity f is the only variable that is regularized. In all the other examples, strain hardening is incorporated into the material behavior, and convergence of the global response is significantly faster.

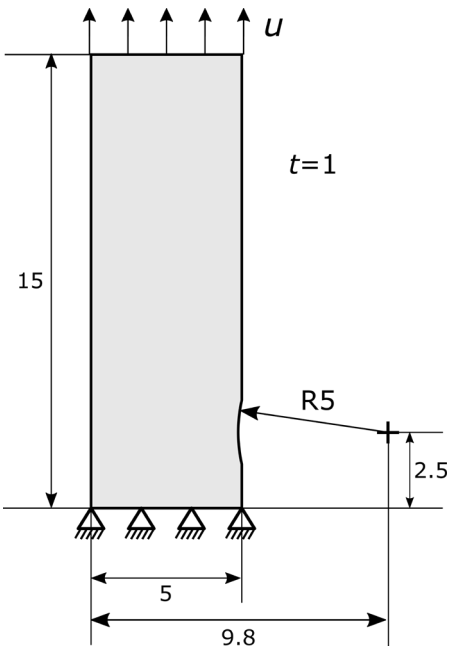

Figure 1. Plane-strain tension specimen with geometrical imperfection to trigger an inclined shear band for a non-hardening matrix material.

Table 1. Material parameters used in the simulation of shear banding under plane-strain tension.

Elasticity and yielding						
E (GPa)			ν		σ_0 (MPa)	
210			0.3		400	
Porous plasticity						
q_1	q_2	q_3	f_0	f_C	f_F	k_S
1.5	1.0	2.25	0.025	0.04	0.12	1.4

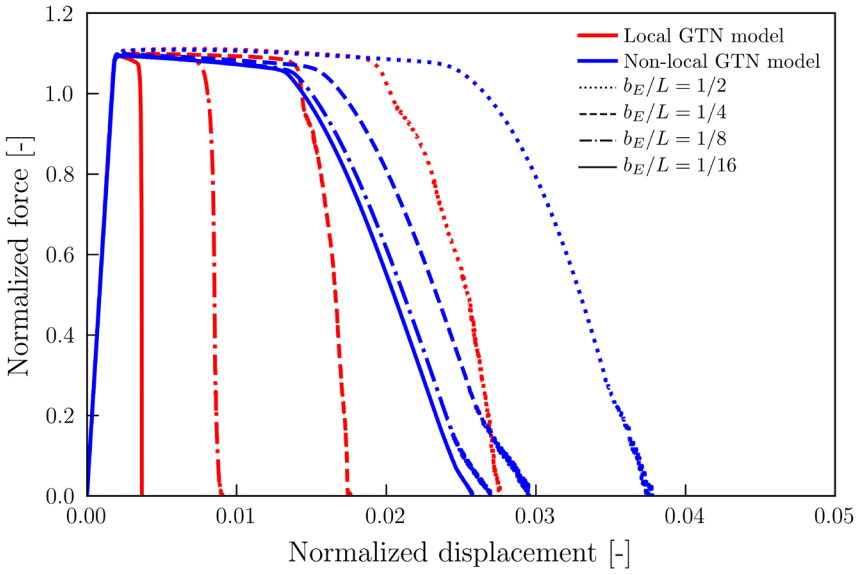

Figure 2. Global response of the plane-strain tension specimen obtained in simulations using the local and non-local GTN model for a non-hardening matrix material, where b_E is the element width and L is the material characteristic length.

Figure 2 shows the global response of the plane-strain tension specimen in simulations with the local and non-local Gurson model upon mesh refinement, b_{E} being the mesh size and L the material characteristic length. The normalized force is calculated as $F/(\sigma_0 A_0)$, where F is the resultant force and A_0 is the initial minimum area of the specimen, i.e., measured at the height of the center of the geometrical imperfection. The normalized displacement is defined as u/H_0, where u is the prescribed displacement and H_0 is the initial height of the specimen. Local and non-local global responses for four uniform meshes are simulated, ranging from 14 elements to 112 elements across the width of the specimen. In Figure 2, the red curves labeled 'local' indicate that the local GTN model (i.e., the material characteristic length L is equal to zero) is used, whereas the blue curves labeled 'non-local' designate that the non-local GTN model is used. The material characteristic length L is then kept constant with successive mesh refinements. The material is modelled with void coalescence at f_{C} and ultimately element erosion when the porosity has reached $0.98f_{\mathrm{F}}$. The decrease in load-carrying capacity all the way down to

$F \approx 0.2\sigma_0 A_0$ in Figure 2 is due to void coalescence, while the final drop down to zero is caused by element erosion and crack propagation. The local simulations are clearly very mesh sensitive, while the non-local simulations evidently converge towards a mesh-insensitive response. It is up for discussion whether the finest mesh has fully converged or not, but it is apparent from the trend shown in Figure 2 that the next mesh refinement would have been practically identical to the response predicted for $b_E/L = 1/16$. The b_E/L-ratio needed to obtain a converged non-local (i.e., fully mesh-independent) response, will depend on the gradients of the porosity in the problem at hand, and as will be shown in the next example, strain hardening will result in significantly faster convergence.

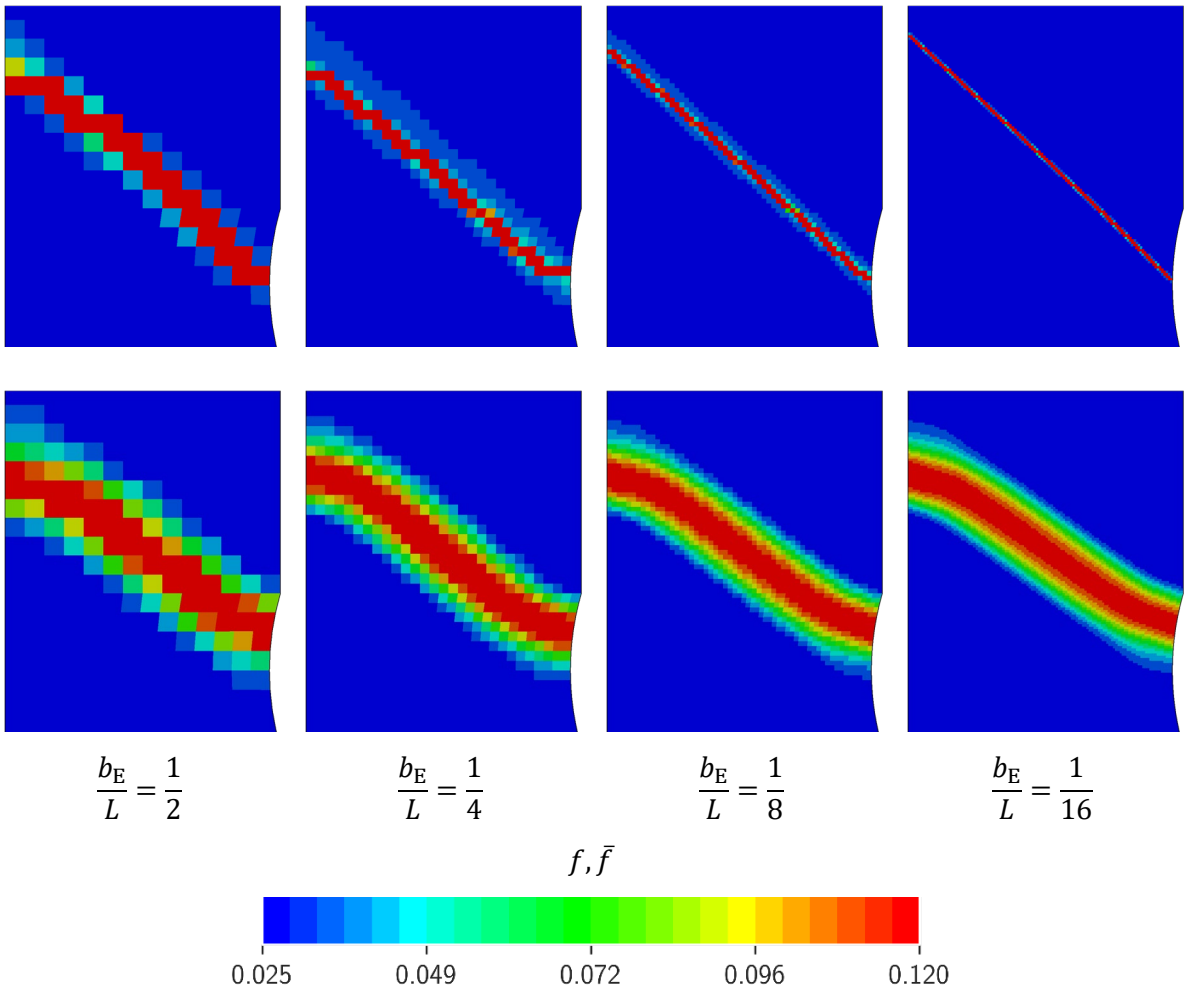

Figure 3. Local (upper row) and non-local (lower row) porosity fields for successive mesh refinements from the simulations of shear banding in the plane-strain tension specimen for a non-hardening matrix material.

Figure 3 shows plots of the porosity, namely f in local simulations and $\bar{f}$ in non-local simulations, for a fully fractured specimen on the undeformed quadrilateral mesh. In each simulation, the porosity is plotted at the termination point of the computed global force vs displacement curves shown in Figure 2. In the local simulations, the shear band width is clearly determined by the mesh size. In the non-local simulations on the other hand, the shear band width is mesh insensitive, and rather determined by the incorporated material characteristic length. There are significant gradients in the strain and porosity across the specimen, and the resolution of these gradients improves with increasing mesh refinement. The good agreement between the predicted distributions of the non-local porosity in the three finest meshes when using the non-local GTN model is evident. This finding implies that a converged distribution of the non-local porosity is obtained already at $b_{\mathrm{E}}/L = 1/4$.

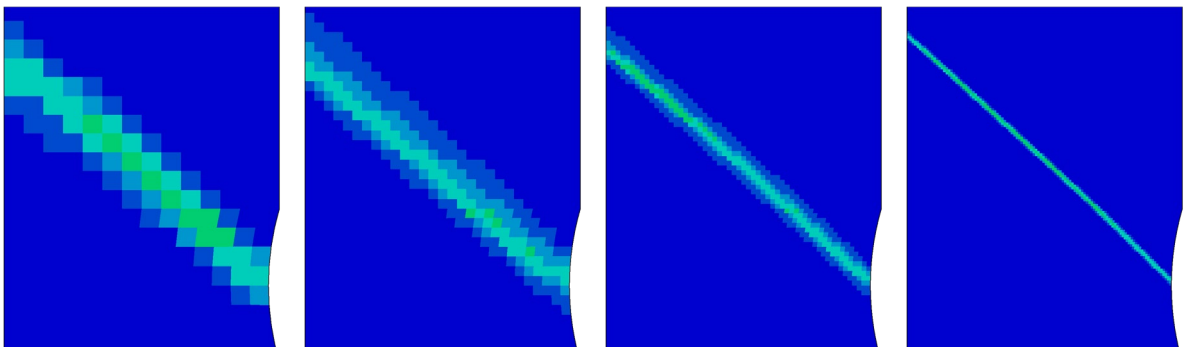

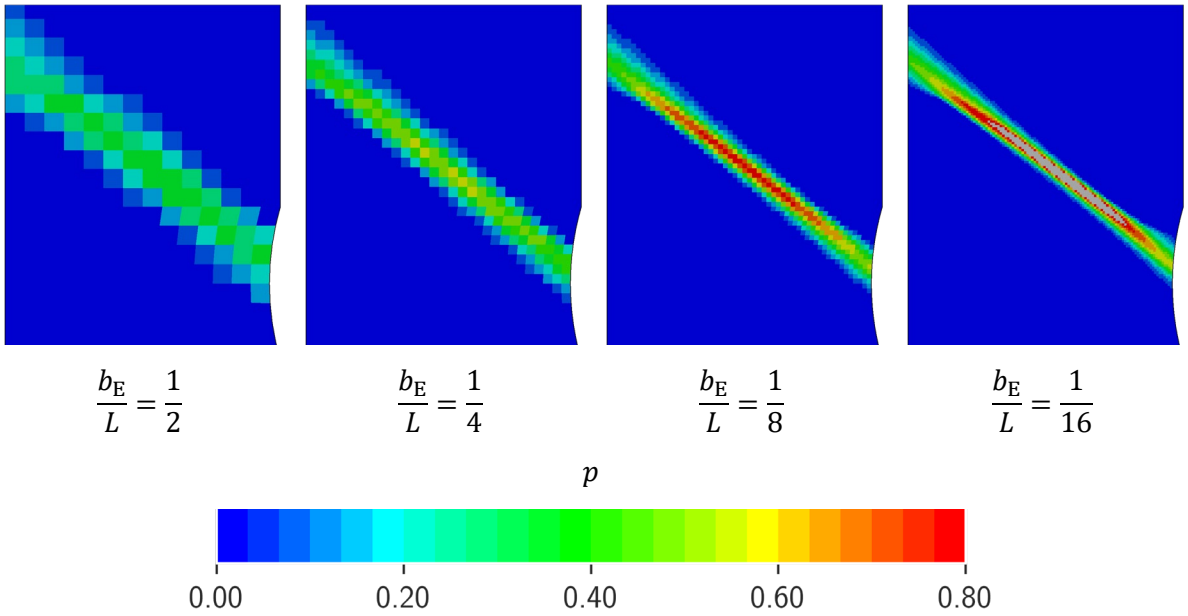

Figure 4. Local (upper row) and non-local (lower row) equivalent plastic strain fields for successive mesh refinements from the simulations of shear banding in the plane-strain tension specimen for a non-hardening matrix material.

Figure 4 shows plots of the equivalent plastic strain p for a fully fractured specimen on the undeformed quadrilateral mesh. In the local simulations, the equivalent plastic strain localizes as the mesh is refined in a similar way as the porosity. In the non-local simulations, the equivalent plastic strain increases markedly in the center of the shear band as the mesh is refined, whereas the width of the plastic zone decreases more slowly. The reason for this lack of convergence is the combination of a non-hardening matrix material with regularization only of the rate of change of the porosity. This results in significantly slower convergence of the global response compared to simulations with strain hardening, as will be demonstrated in all succeeding examples.

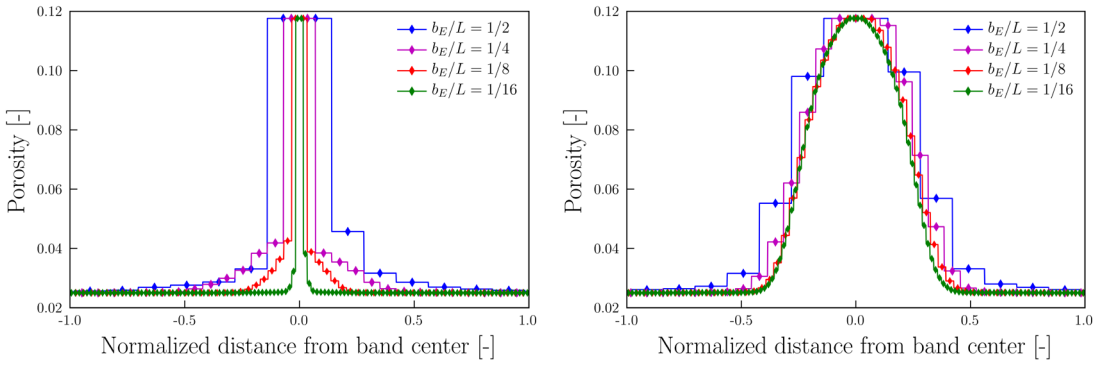

Figure 5. Distributions of the porosity across the shear band in the plane-strain tension specimen from local (left) and non-local (right) simulations for a non-hardening matrix material.

Figure 5 presents the distribution of the porosity across the shear band with mesh refinement as predicted by the local and non-local GTN model. The values are shown along a vertical section through the middle of the specimen. The peak values are equal to $0.98f_{\mathrm{F}}$, at which element erosion occurs. The shear band in the simulations with the local GTN model lies along a 45 degree line, which is the reason for the band width of two elements at failure: any vertical section through a rectangular quadrilateral mesh contains two failed elements if the shear band is to follow a 45 degree angle, as the crack must propagate through a horizontal and then a vertical neighbor element successively. The strong sensitivity of the band width on the mesh resolution in the simulations with the local GTN model is evident. As already shown in Figure 3, the width of the band is determined by the element size in the local simulations, and for the most refined mesh, almost the entire specimen undergoes purely elastic deformation.

As the mesh is refined in the non-local simulations, it is interesting to note not only the convergence of the spatial distribution of the porosity, but also that the width of the crack propagation converges as well, as illustrated by the number of elements that reach $f = 0.98f_F$ and are thus eroded. As can be seen from Figure 5, the crack is two elements wide

for the coarsest mesh ($b_E/L = 1/2$), and then as the mesh is refined the crack has a width of three elements for $b_E/L = 1/4$, four elements for $b_E/L = 1/8$ and seven elements for $b_E/L = 1/16$. As the mesh is refined, it is apparent that the crack width converges towards a width determined by the material characteristic length L.

This spurious element erosion in the wake of the crack tip should be addressed. It is due to the non-local averaging of the porosity increment in all elements, not only those undergoing plastic deformations. Upon mesh refinement the width of the plastic zone decreases, thus the non-local averaging of the porosity increment in elastic elements as well is necessary in order to obtain convergence of the global response as the mesh is refined. The implication is that elements in the wake of the crack will experience a positive increment in porosity as long as they are sufficiently close to the crack tip, where this distance is controlled by the b_E/L-ratio and the coefficients p_w and q_w in the weight function. The fact that the crack has a finite width defined by L has no consequences for the global response, as the crack has already passed before this phenomenon occurs.

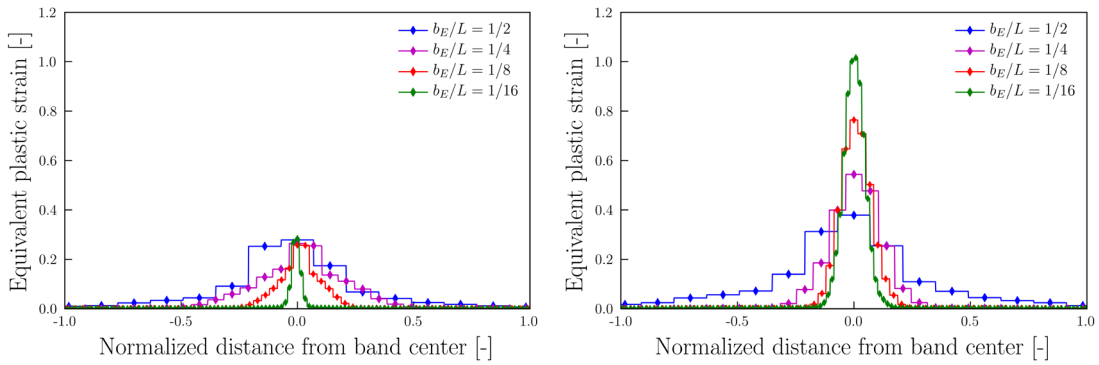

Figure 6. Distributions of the equivalent plastic strain across the shear band in the plane-strain tension specimen from local (left) and non-local (right) simulations for a non-hardening matrix material.

Figure 6 shows the distribution of the equivalent plastic strain across the shear band of a fully fractured specimen for the simulations with the local and non-local GTN models. In the local simulations, the maximum value of the equivalent plastic strain decreases slightly upon mesh refinement, which is most likely due to a slight increase in the stress triaxiality in the critical element in the center of the shear band with mesh refinement, resulting in slightly faster void growth. Figure 6 illustrates how the distribution of the equivalent plastic strains across the band predicted by the local GTN model gets narrower as the mesh is refined, resulting in less global deformation before element erosion, indicating that immediate failure would occur when reaching plasticity with an infinitely refined mesh.

In the non-local simulations, it is evident that the maximum value attained for the equivalent plastic strain differs significantly between the meshes, and that much larger peak values are reached than in the simulations with the local GTN model. As mentioned previously, this is caused by the lack of strain hardening and the fact that only the porosity is regularized in the non-local GTN model. With increasing maximum value, the distribution of the equivalent plastic strain becomes steadily narrower. As already mentioned, the result of this lack of convergence of the plastic deformation is a markedly slower convergence of the global response. To avoid this problem, also the equivalent plastic strain would have to be regularized in a similar manner as the porosity.

3.2 Shear banding in strain hardening material

We will now investigate the importance of including strain hardening when regularizing the damage parameter (in contrast to the plastic strain) in a non-local constitutive model. The simulations of the shear band specimen demonstrated rather slow convergence in

the global response. Across the shear band, the peak value and the distribution of the equivalent plastic strain did not converge with mesh refinement even for the non-local GTN model. We will now demonstrate that by introducing strain hardening this issue is resolved.

The plane-strain tension specimen with geometric imperfection and the displacement-controlled loading used in the simulations of shear banding with a strain hardening material are shown in Figure 7. The material parameters of the GTN model adopted in this example are summarized in Table 2. Note that the value of k_S used in this example is outside the range suggested by Nahshon & Hutchinson (2008), and was given this high value to limit the element distortion that occurred towards fracture for the coarsest mesh. The specimen geometry is changed compared to the previous example to ensure an inclined shear band with the given material parameters. In addition, a mixed-mode loading giving combined tension and shear is applied to the specimen.

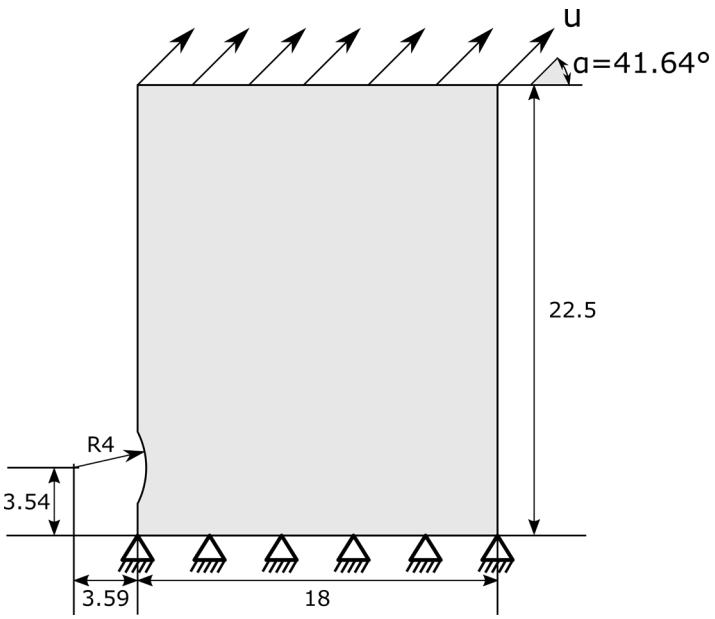

Figure 7. Plane-strain tension specimen with geometrical imperfection to trigger an inclined shear band for a strain-hardening matrix material.

Table 2. Material parameters used in the simulation of the plane-strain tension specimen with a strain-hardening matrix material.

Elasticity and initial yielding							
E (GPa)		ν		σ_0 (MPa)			
210		0.3		400			
Strain hardening							
Q_1 (MPa)	C_1	Q_2 (MPa)	C_2	Q_3 (MPa)	C_3		
28.6	11.3	101.8	1.4	2823.5	0.07		
Porous plasticity							
q_1	q_2	q_3	f_0	f_C	f_F	k_S	A_N
1.5	1.0	2.25	0.01	0.025	0.12	5.0	0.040

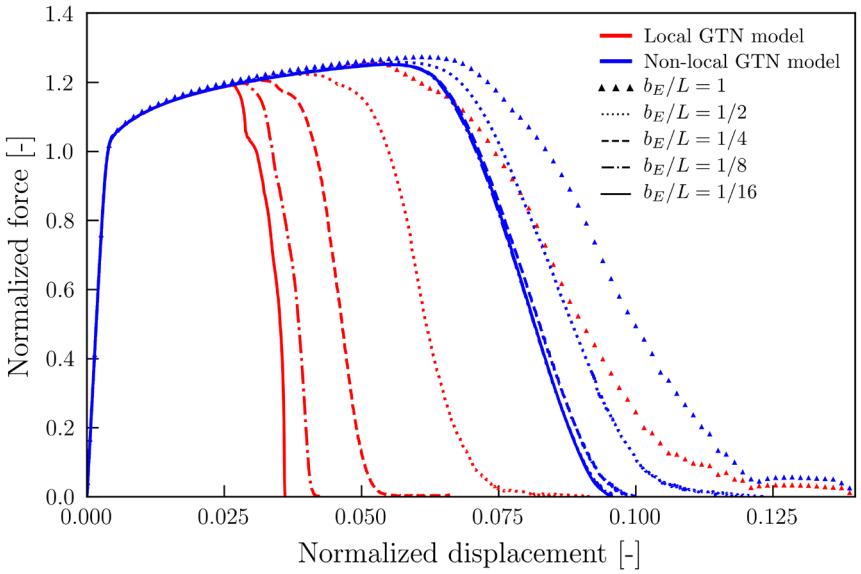

Figure 8. Global response of the plane-strain tension specimen from simulations with the local and non-local GTN model and various mesh sizes for a strain-hardening matrix material.

The normalized force-displacement curves from simulations with the local (red curves) and non-local (blue curves) GTN models are shown in Figure 8 for five different mesh sizes. The normalized force is calculated as $F/(\sigma_0 A_0)$, where F is the resultant force and

A_0 is the initial minimum area of the specimen. The normalized displacement is defined as u/H_0, where u is the prescribed displacement (as indicated in Figure 7) and H_0 is the initial height of the specimen. As is evident, the local simulations exhibit severe mesh dependency, while the global response obtained in the non-local simulations converges rapidly upon mesh refinement. The non-local solutions for mesh size $b_E/L = 1/8$ and $b_E/L = 1/16$ are both shown, but the global response curves are simply on top of each other, and also the solution for mesh size $b_E/L = 1/4$ has practically converged. Note here that the local and non-local solutions are not identical for $b_E/L = 1$. For this to happen, b_E/L has to be slightly larger than unity with the given parameters p_w and q_w of the weight function used in the non-local integral.

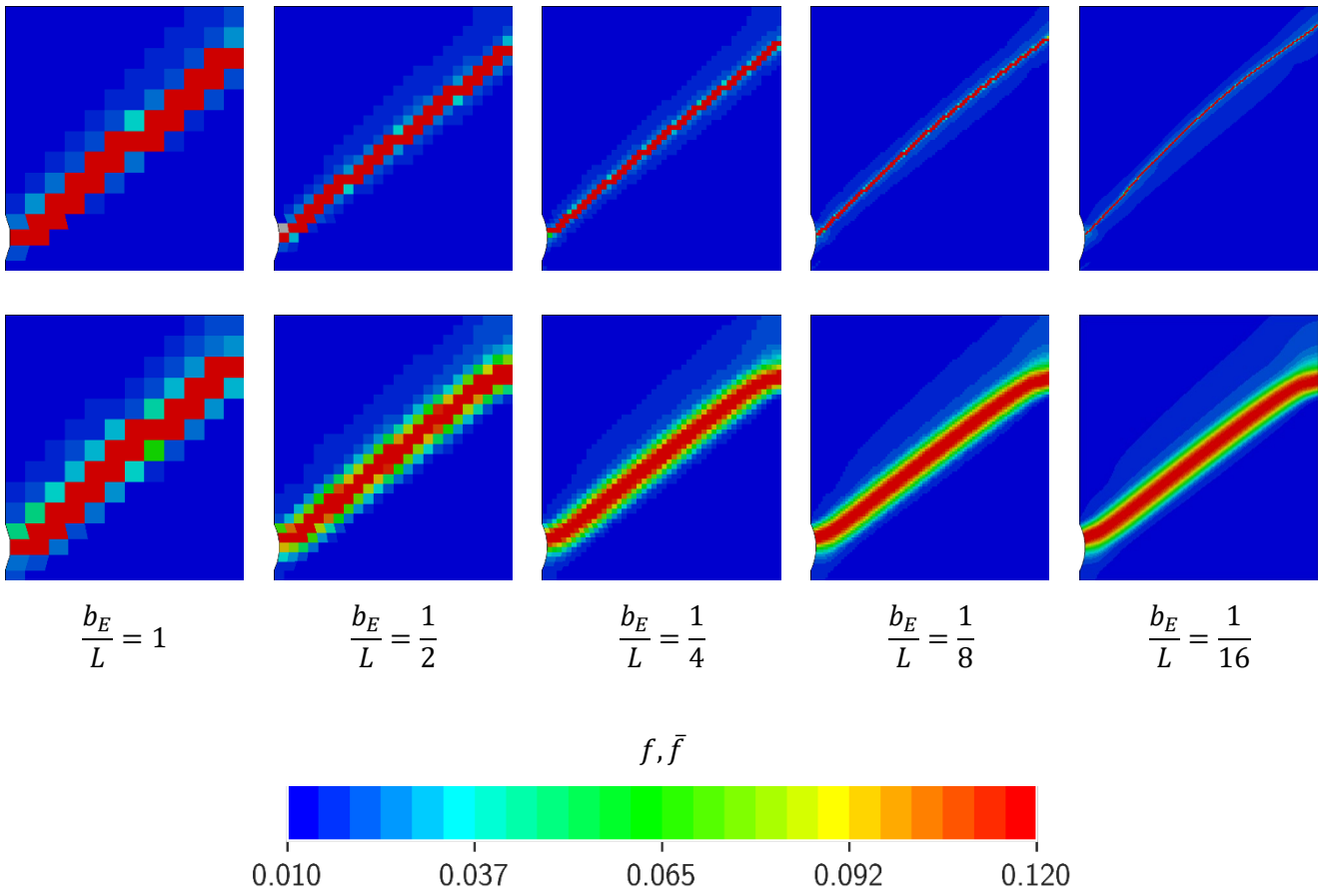

Figure 9. Local (upper row) vs non-local (lower row) porosity fields for successive mesh refinements from the simulations of the plane-strain tension specimen for a strain-hardening matrix material.

Figure 9 compares the porosity fields predicted by the local and non-local GTN models. In both cases, an inclined band of high porosity is predicted. As expected, for the local GTN model, the band width is determined by the mesh size, while for the non-local GTN model, the band width converges to a value determined by the material characteristic length. Comparisons of the predicted equivalent plastic strain fields by the local and non-local GTN models are given in Figure 10. It is evident that by including strain hardening, the maximum values of the equivalent plastic strain converge with mesh refinement and this is the reason for the much faster convergence of the global response.

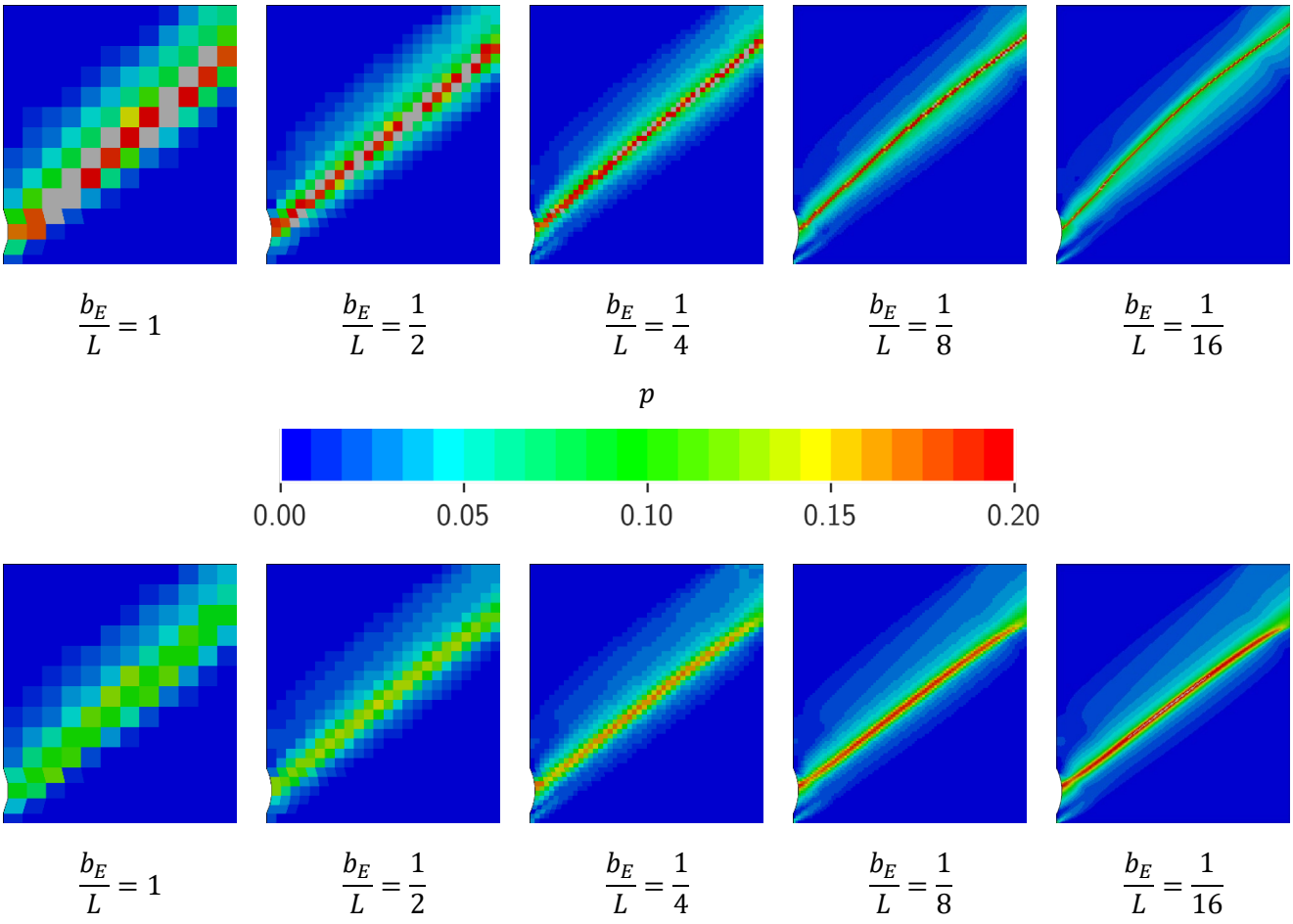

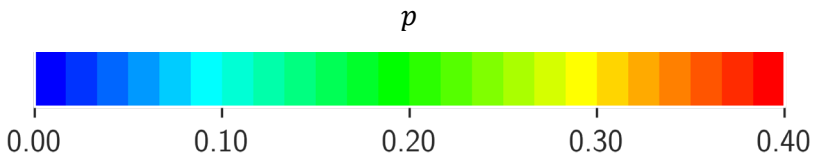

Figure 10. Local (upper row) vs non-local (lower row) equivalent plastic strain fields for successive mesh refinements from the simulations of the plane-strain tension specimen for a strain-hardening matrix material.

Figure 11 and Figure 12 present in turn the distributions of the porosity and the equivalent plastic strain along a vertical section slightly to the right of the middle of the specimen across the localization band. The left and right sides of the figures correspond to elements below and above the band, respectively. It is seen from these figures that the band width continuously decreases in the local simulations, while it quickly converges in the non-local simulations. This conclusion holds both for the porosity and the equivalent plastic strain, even if the former seems to converge more rapidly. Recall that the peak value and the width of the equivalent plastic strain distribution did not converge with mesh refinement in the case of a non-hardening matrix material. We can also note the asymmetric response of the specimen in Figure 12 , i.e., how the distribution of the equivalent plastic strain on either side of the crack differs.

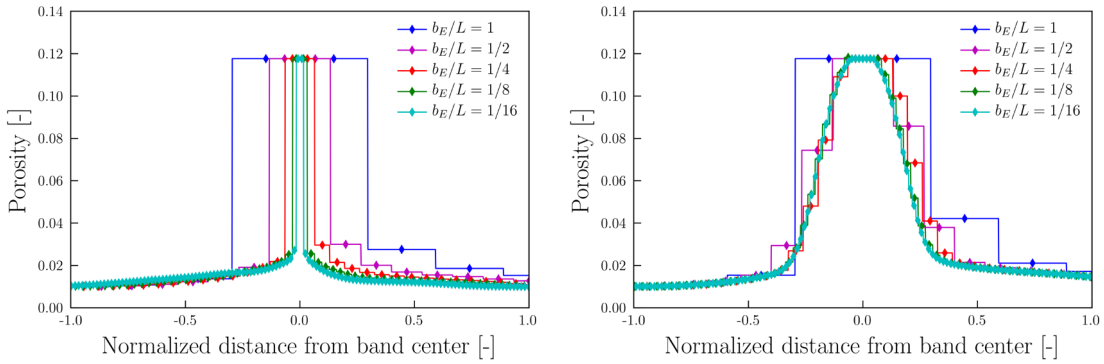

Figure 11. Distributions of the porosity along a vertical section across the plane-strain tension specimen from local (left) and non-local (right) simulations for a strain-hardening matrix material.

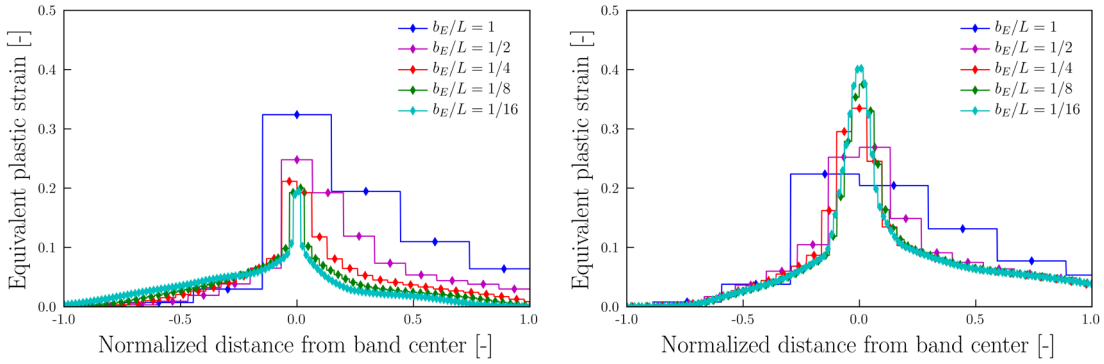

Figure 12. Distributions of the equivalent plastic strain along a vertical section across the plane-strain tension specimen from local (left) and non-local (right) simulations for a strain-hardening matrix material.

3.3 Crack propagation in strain hardening material

We will now focus on crack initiation and propagation, by simulating a typical compact tension (CT) specimen under plane-strain conditions. The specimen geometry and the displacement-controlled loading are presented in Figure 13 and material parameters are given in Table 3. The material has the same strain-hardening parameters as in the previous example, while the parameters controlling the damage evolution have been changed.

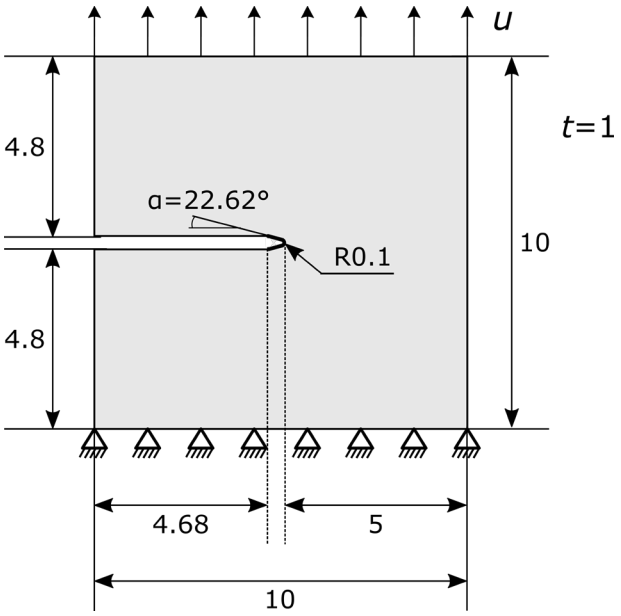

Figure 13. Geometry of the compact-tension (CT) specimen.

Table 3. Material parameters used in the simulation of the compact-tension (CT) specimen.

Elasticity and initial yielding					
E (GPa)		ν		σ_0 (MPa)	
210		0.3		400	
Strain hardening					
Q_1 (MPa)	C_1	Q_2 (MPa)	C_2	Q_3 (MPa)	C_3
28.6	11.3	101.8	1.4	2823.5	0.07
Porous plasticity					
q_1	q_2	q_3	f_0	f_C	f_F	k_S
1.5	1.0	2.25	0.02	0.04	0.10	0

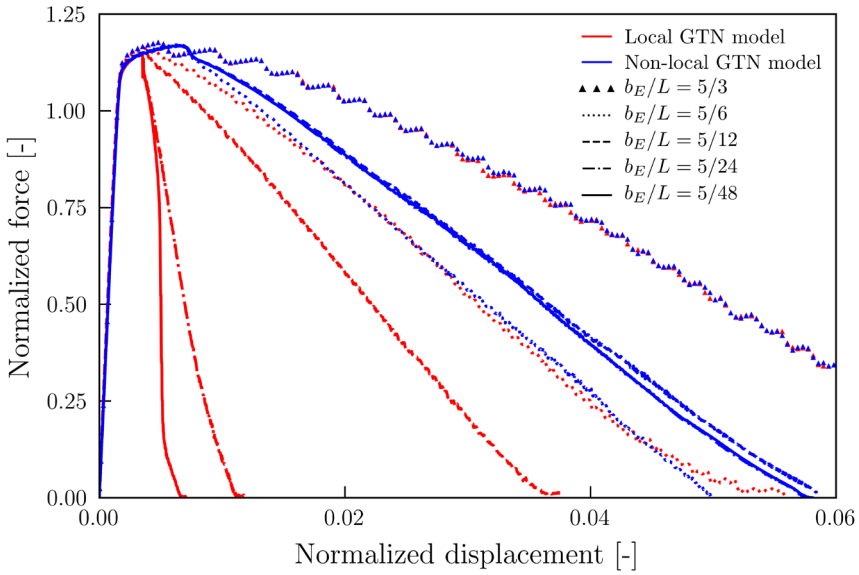

Figure 14. Global response of the CT specimen from simulations with the local and non-local GTN models and various mesh sizes.

Figure 14 shows the normalized force-displacement curves obtained for the CT specimen in simulations with the local (red curves) and non-local (blue curves) GTN models and various mesh sizes. The normalized force is calculated as $F/(\sigma_0 A_0)$, where F is the resultant force and A_0 is the initial minimum area of the specimen. The normalized displacement is defined as u/H_0, where u is the prescribed displacement and H_0 is the initial height of the specimen. The curve labeled $b_E/L = 5/3$ corresponds to the coarsest mesh and is almost identical for both the local and non-local simulations. As the element size b_E is larger than the material characteristic length L, there is practically no interaction between elements. This way we can study how the global response converges, starting from a completely local response. The numerous sudden drops in the force for the coarser mesh are due to element erosion. Because of the large element size, the erosion of an element leads to a visible drop in the force. As the element size is reduced and becomes small compared to the total width of the specimen, the force drop caused by the erosion of an element becomes negligible and the response curves appear smooth. As the mesh is refined, we can see how the global response obtained by the non-local GTN model quickly converges, while the simulations with the local GTN model once again exhibit significant mesh dependency both with respect to crack initiation and crack propagation speed (given by the slope of the curves in the post-peak regime). In the non-local simulations, the global response has basically converged for $b_E/L = 5/12$. The rapid convergence of the global response is most likely due to a combination of the incorporation of strain hardening, less pronounce strain gradients and a better alignment of the fracture path with the quadrilateral mesh.

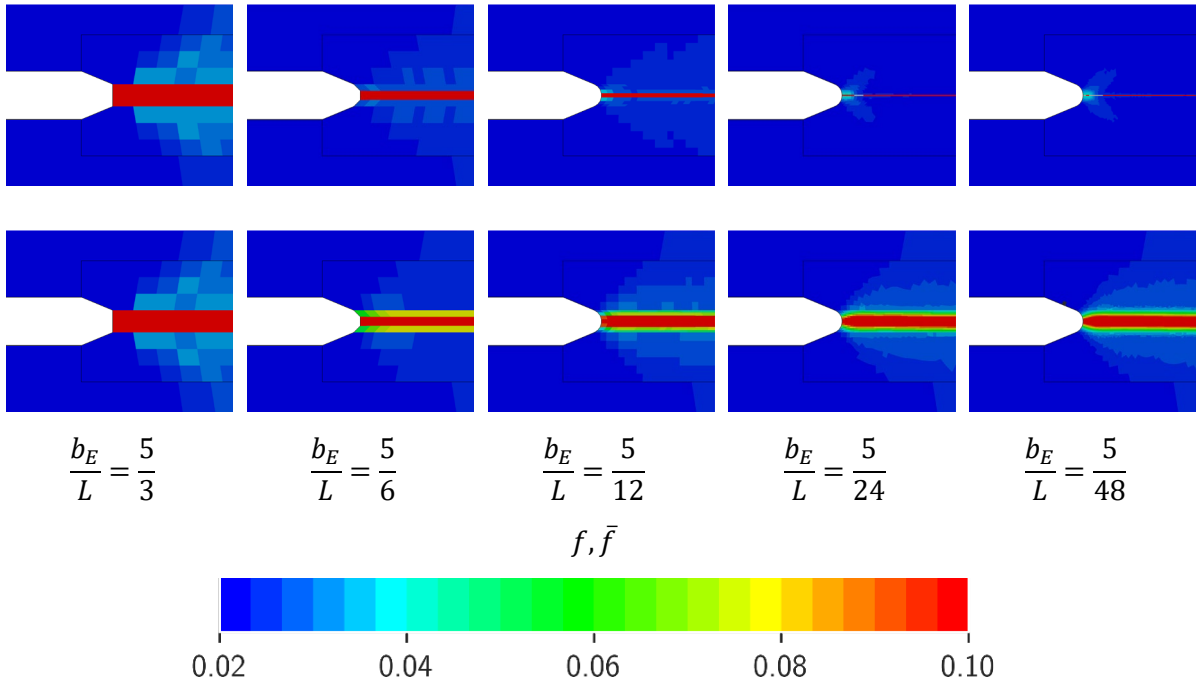

Figure 15. Local (upper row) and non-local (lower row) porosity fields around the crack tip for successive mesh refinements from the simulations of the CT specimen.

Figure 15 shows the local and non-local porosity fields for the fully fractured specimen plotted on the initial configuration. With the local GTN model, the crack propagates through a single row of elements, resulting in severe mesh dependency. In contrast, when using the non-local GTN model, it is evident that the porosity field, like the global response, has basically converged for $b_E/L = 5/12$. From Figure 14, it is apparent that for the first mesh refinement, $b_E/L = 5/6$, the local and non-local simulations give similar results, but the predicted force level in the non-local simulation is in fact below the force level at convergence. By considering the porosity field in the non-local simulation in Figure 15, we find that although the porosity is more spatially distributed than in the local simulation, the crack still propagates through a single element. The b_E/L-ratio is not yet sufficiently small to result in crack propagation across several elements, which results in the local and non-local predictions being very similar. This illustrates a

rather interesting phenomenon, namely that the non-local solution not always exhibits monotonic convergence in the global response. The obtained non-local solutions will converge towards a mesh-independent solution with mesh refinement, but how the solution converges depends on the problem at hand. In the non-local model, the width of the crack is, as expected, determined by the material characteristic length and not the mesh, and both the spatial distribution of the porosity and the width of the propagating crack (measured in terms of the number of deleted elements) converge towards a mesh-independent solution.

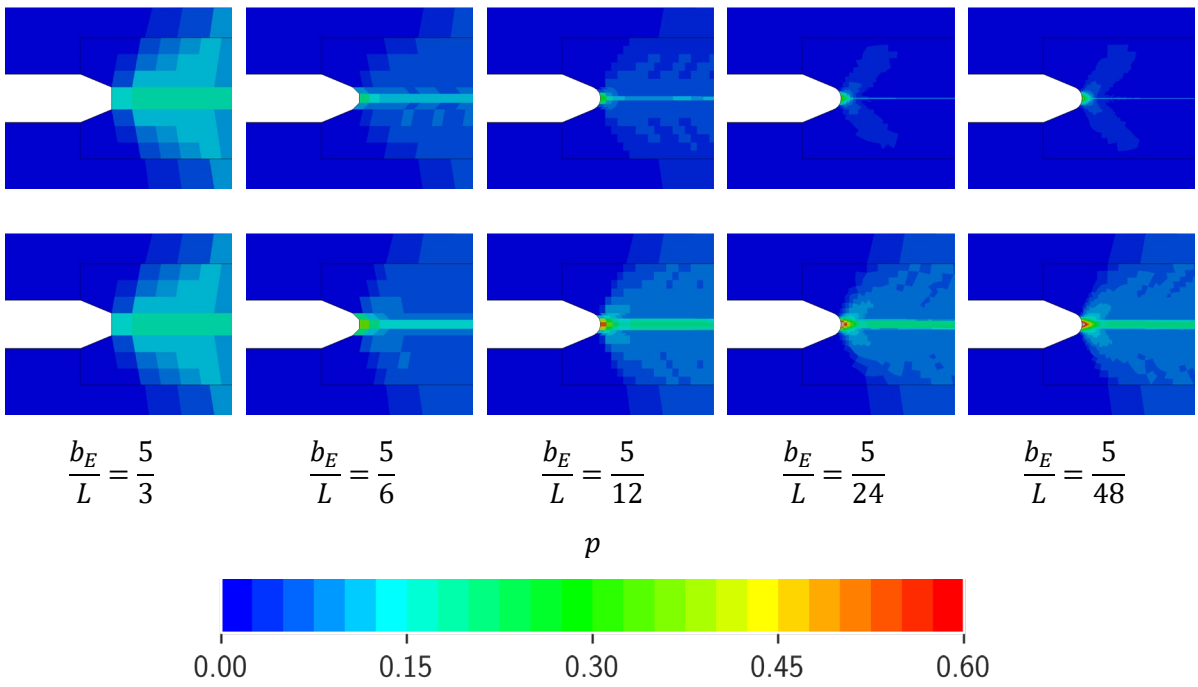

Figure 16. Local (upper row) and non-local (lower row) equivalent plastic strain fields around the crack tip for successive mesh refinements from the simulations of the CT specimen.

Figure 16 shows the equivalent plastic strain fields obtained in the local and non-local simulations for the fully fractured specimen plotted on the initial configuration. With the local GTN model, the plastic zone decreases rapidly in size with mesh refinement and except for a limited spatial distribution before crack initiation occurs, the crack propagates for very small plastic strains. There is almost no plastic strain outside the critical elements that fail during the crack propagation. The equivalent plastic strain fields obtained with the non-local GTN model are practically identical for $b_E/L \leq 5/12$, which is consistent with the observed convergence of the global response.

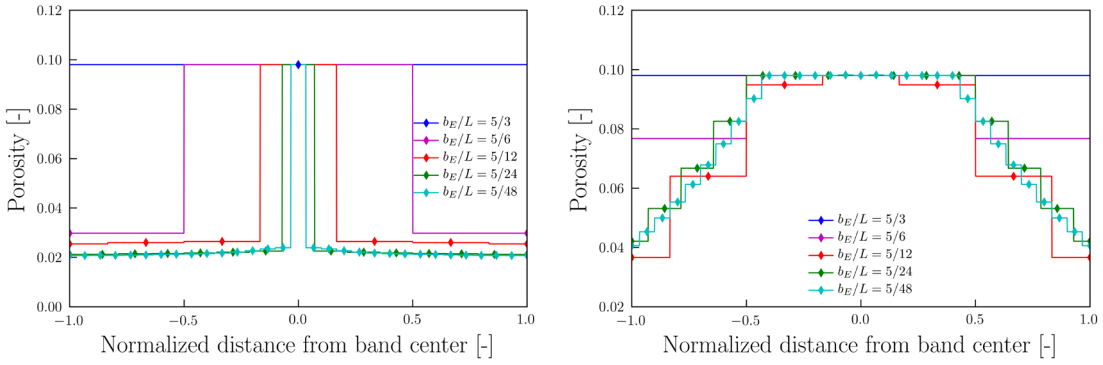

Figure 17. Distributions of the porosity across the deformation band in the CT specimen from local (left) and non-local (right) simulations.

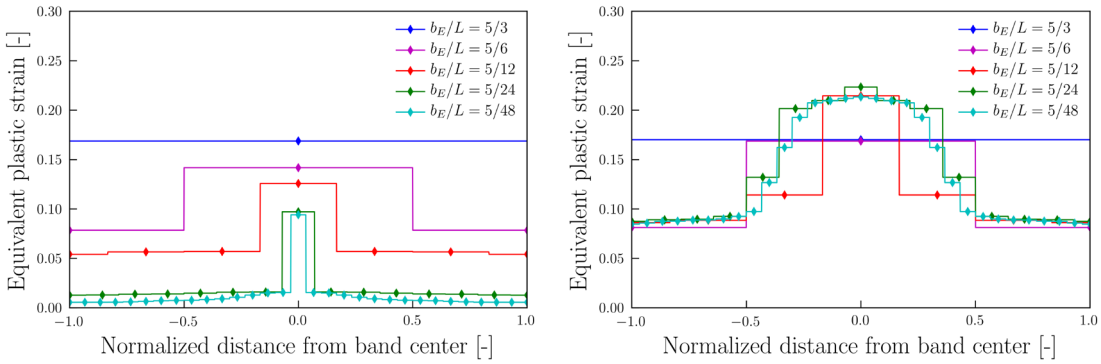

Figure 18. Distributions of the equivalent plastic strain across the deformation band in the CT specimen from local (left) and non-local (right) simulations.

Figure 17 illustrates the distribution of the porosity across the deformation band in the CT specimen. In the local simulations, the width of the band is defined by the mesh size, as in the previous examples, whereas in the non-local simulations, the spatial distribution of the porosity and the crack width converge rapidly. The distribution of the equivalent plastic strain across the deformation band obtained in the local and non-local simulations is displayed Figure 18. As for the porosity, the band width predicted by the local GTN model decreases with mesh refinement, localizing into the smallest possible width determined by the mesh. Owing to the strain hardening of the matrix material, the peak value of the equivalent plastic strain and the width of the localization band predicted by the non-local model converge rapidly with mesh refinement.

This example is inspired by Needleman & Tvergaard (1998), who reported on lack of convergence in the predictions of crack initiation and propagation in a similar specimen by use of a non-local GTN model. In fact, they found that the non-local simulations were only slightly less mesh-sensitive than the corresponding local simulations and argued that a finer mesh relative to the material characteristic length might be needed to resolve the localization of deformation in the near crack-tip region. As mentioned in Section 2.3, another possible explanation for the lack of convergence might be the use of the

incremental update of the non-local porosity defined by Equation (12). By adopting instead the incremental update given by Equation *(13)*, we were able to get results that converged both with respect to the global response of the CT specimen and the local response of the critical element that fails first. The fast global convergence with mesh refinement for the CT specimen suggests that the exact b_{E}/L-ratio at which mesh-insensitive results are obtained depends not only on the material parameters, but also the strain gradients in the FE model. The strain gradients occurring in the CT specimen seem to be easier to resolve, perhaps because the crack propagation path perfectly lines up with the rectangular quadrilateral mesh.

3.4 Tensile ductility and the problem of excessive regularization

We will now address the problem of excessive regularization reported in the literature and show that it is caused by using a fixed instead of an updated element interaction matrix in the evaluation of the non-local integral. A cylindrical specimen in uniaxial tension is considered for this purpose. The specimen geometry is shown in Figure 19 and material parameters used are given in Table 4. In the following, we compare results by the local and non-local GTN models by evaluating the non-local integral either on the reference configuration, using a fixed element interaction matrix, or on the current configuration, using an updated element interaction matrix. In the former case, the element interaction matrix is calculated once at the start of the simulation, while in the latter case, it is updated at every time step to account for changes in geometry. In contrast to the previous examples, the material parameters were chosen to give a significantly ductile response, since the differences between the fixed and updated non-local GTN models only become important at large deformations. The cylindrical specimen is

modelled as a three-dimensional (3D) part, with three symmetry planes, and thus only 1/8 of the specimen is modelled. Five mesh resolutions will be used, ranging from 9 to 45 elements across the radius.

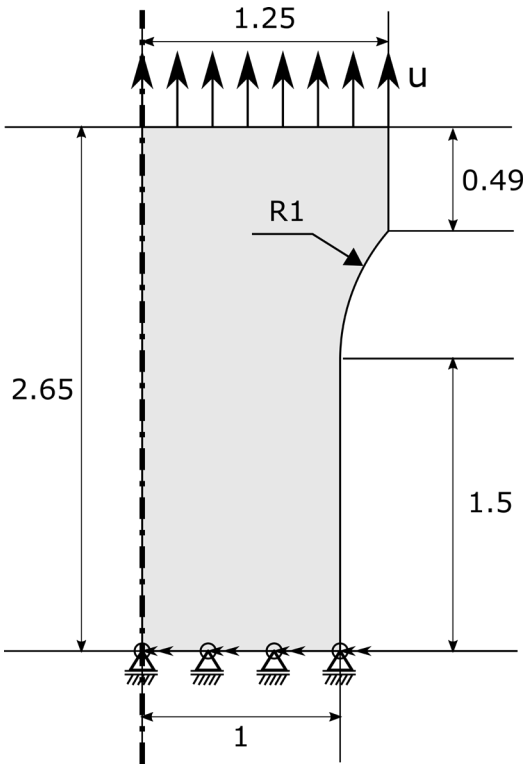

Figure 19. Geometry of the cylindrical tensile specimen.

Table 4. Material parameters applied in simulations of tensile ductility.

Elasticity and initial yielding							
E (GPa)			ν		σ_0 (MPa)		
210			0.3		400		
Strain hardening							
Q_1 (MPa)	C_1		Q_2 (MPa)	C_2	Q_3 (MPa)	C_3	
28.6	11.3		101.8	1.4	2823.5	0.07	
Porous plasticity							
q_1	q_2	q_3	f_0	f_C	f_F	k_S	A_N
1.5	1.0	2.25	0.002	0.10	0.20	0.0	0.0

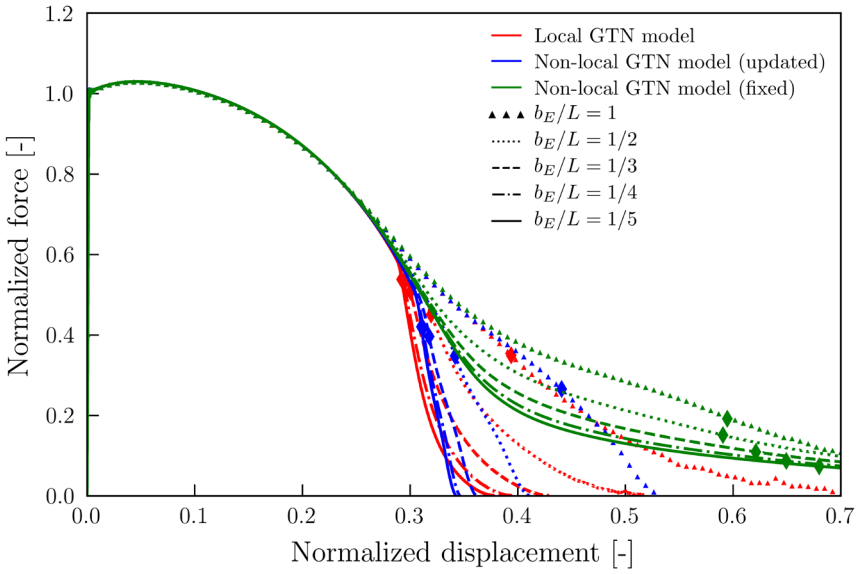

Figure 20. Global response of the cylindrical tensile specimen

The global response of the cylindrical tensile specimen is shown in Figure 20. The normalized force is calculated as $F/(\sigma_0 A_0)$, where F is the resultant force and A_0 is the initial area of the specimen's gauge section. The normalized displacement is defined as u/H_0, where u is the prescribed displacement and $2H_0$ is the initial height of the specimen. The response of the local GTN model is shown by red curves, whereas the responses of the fixed and updated non-local GTN models are shown by green and blue curves, respectively. The point marked by a diamond in each curve corresponds to first element failure in the center of the specimen. From the figure, it is seen that it is only the updated non-local GTN model that is able to describe both crack initiation and propagation in a realistic way, i.e., that the response curve drops steeply after first fracture and until the specimen is fully fractured, which is the typical response seen in tensile tests. Thus, this model will be used as a baseline in the discussion of the two other models. The fixed non-local GTN model gives very poor results both with respect to crack initiation and propagation. Fracture initiates rather late in the simulations and there is hardly any change in the response after the first element fails. The reason for this is that

there is hardly any crack propagation predicted with this model. The local GTN model predicts initiation somewhat early because of the lack of regularization. What is more interesting is that the local GTN model is not able to predict the expected steep decent of the response curve after first fracture and until the specimen is fully fractured, i.e., the crack speed slows down towards full fracture. The reason for this response is that during the crack propagation, the critical element (i.e., the next element to fail) has significantly larger porosity than its neighbors. As the crack initiates in the center and propagates outwards, each element that is eroded starts from a low porosity that increases towards the critical value. The damage is not spread outwards in front of the crack, and this lack of a "process zone" in front of the crack reduces the crack propagation speed in an unphysical manner. The updated non-local GTN model, on the other hand, captures the process zone ahead of the crack, and a practically constant crack speed (i.e., the tangent to the response curve) is obtained.

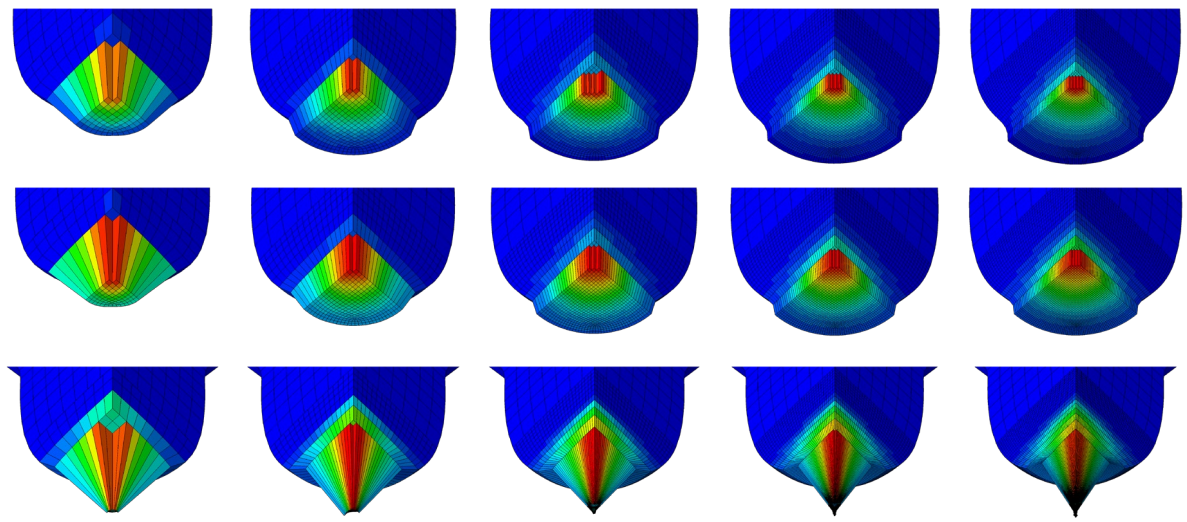

$\frac{b_E}{L} = 1$ $\frac{b_E}{L} = \frac{1}{2}$ $\frac{b_E}{L} = \frac{1}{3}$ $\frac{b_E}{L} = \frac{1}{4}$ $\frac{b_E}{L} = \frac{1}{5}$

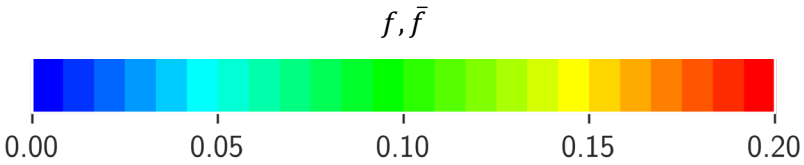

Figure 21. Porosity fields at the time of the first element deletion obtained with the local GTN model (upper row), the updated non-local GTN model (middle row) and the fixed non-local GTN model (lower row) for successive mesh refinements.

Figure 21 shows the porosity fields at first element deletion for the three models with successive mesh refinements. Note that for the coarsest model with $b_E/L = 1$ there is hardly any effects of the non-local regularization and thus the local and non-local GTN models give results that are only slightly different. By comparing the results from the local GTN model (upper row) with those obtained with the updated non-local GTN model (middle row), we find that the porosity is more spatially distributed in the latter model due to the averaging, and this is the reason for the different displacement and force levels at crack initiation predicted with these two models. In the simulations with the fixed non-local GTN model, the specimen has practically no cross-sectional area left at crack initiation due to the large degree of necking that has occurred prior to this event. The large differences in the results obtained with the two version of the non-local GTN model are mostly due to the predicted distribution of porosity in the longitudinal direction of the tensile specimen. As the elements deforms, the updated non-local GTN model only includes elements in the radial direction in the averaging, since the distances between elements in the longitudinal direction become so large that they move outside the averaging domain. In contrast, when using the fixed non-local GTN model no elements move outside the averaging domain as the initial distances are kept throughout the simulation, which results in an excessively regularized solution. These results illustrate that the use of a fixed element interaction matrix in the non-local averaging is only strictly

valid for infinitesimal deformations, and if applied nonetheless for finite deformations excessive regularization could be a severe problem.

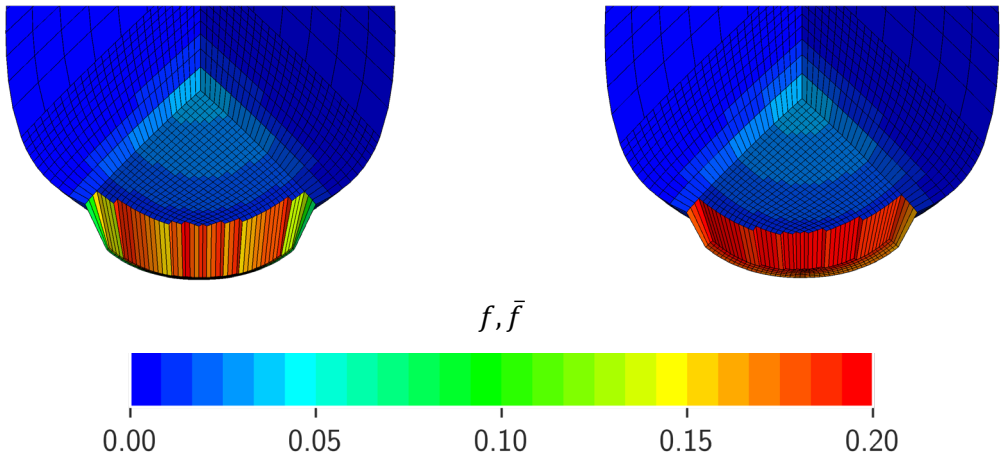

Figure 22. Plots of porosity towards the end of the crack propagation from simulations with the local (left) and updated non-local (right) GTN models ($b_{\mathrm{E}}/L = 1/3$).

Plots of the porosity towards the end of the crack propagation as predicted in local and non-local simulations with mesh size $b_{\mathrm{E}}/L = 1/3$ are compared in Figure 22. Similar results are also obtained for the other mesh sizes. The updated non-local GTN model predicts a higher porosity in front of the propagating crack than the local GTN model. As already mentioned, the more distributed porosity or process zone ahead of the crack is the reason for the more realistic prediction of crack propagation. The unphysically large deformations that induce severe element distortions at the end of the crack propagation in the local simulation are avoided. Figure 22 illustrates an interesting, but perhaps un-intuitive point, namely that the local GTN model gives an overly "regularized" response towards the end of the crack propagation due to element distortion.

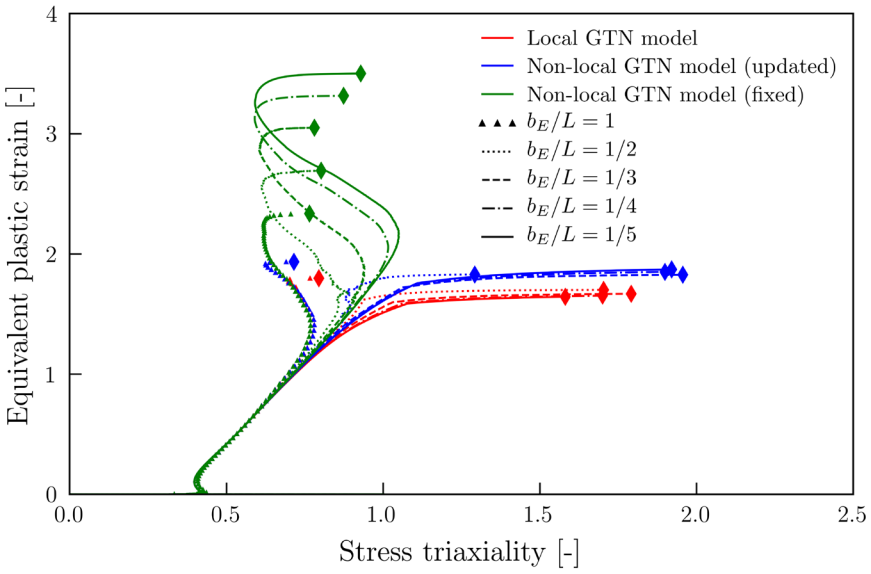

Figure 23. Stress triaxiality vs equivalent plastic strain in the critical element of the uniaxial tensile specimen upon mesh refinements.

Figure 23 shows the stress triaxiality as a function of the equivalent plastic strain in the center element of the cylindrical tensile specimen for all three versions of the GTN model for the different meshes. It transpires that the coarsest mesh is unable to capture the correct response of the specimen and as a result, the stress triaxiality is underestimated at large strains. In the simulations with the fixed non-local GTN model, an erratic evolution of the stress triaxiality is seen with increasing equivalent plastic strain and convergence is not reached in the critical element with the applied mesh refinement. In the simulations with the local GTN model and the updated non-local GTN model, convergence is reached in the equivalent plastic strain at failure of the critical element, which, as discussed for previous examples, is a sign of how fast the global response converges as well. For the latter model, the stress triaxiality at failure of the critical element also converges, while this is not entirely the case in the former.

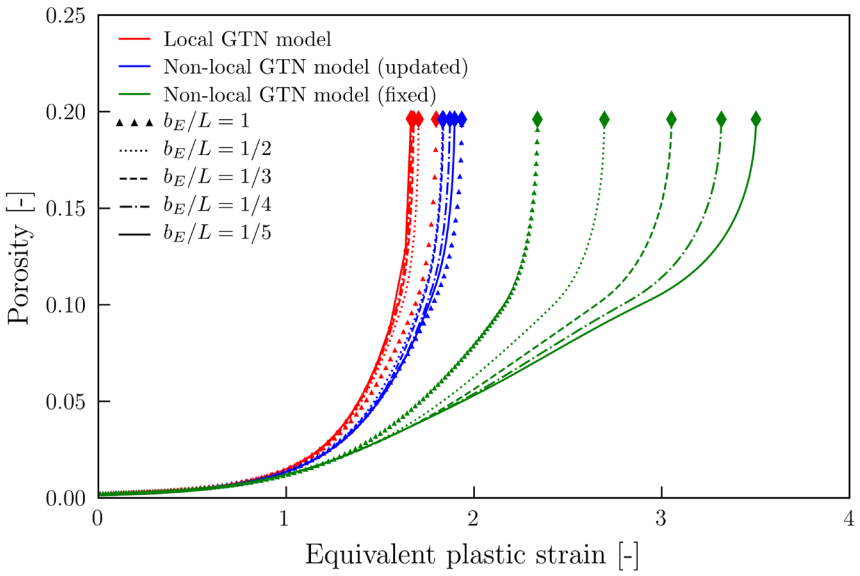

Figure 24. Porosity vs equivalent plastic strain in the critical element of the uniaxial tensile specimen upon mesh refinements.

Figure 24 presents the porosity versus the equivalent plastic strain in the center element of the uniaxial tensile specimen with mesh refinement for the three versions of the GTN model. The fixed non-local GTN model predicts element erosion at significantly higher levels of equivalent plastic strain than the other two GTN models, and there are no apparent signs of convergence locally. Remember that the global response did not converge in simulations with this model either. The small discrepancies for the two other versions of the GTN model are most likely due to the fact that with mesh refinement the centermost element is moved closer to the centerline of the specimen, or that the coarser mesh resolutions are not able to describe the deformation history correctly. No matter which reason holds, the result is that the local evolution of the porosity in the critical element is not subjected to exactly the same deformation history as the mesh is refined. Of primarily interest is still how the fixed non-local GTN model is far from convergence in terms of the response of the critical element.

This example intended to show the necessity of computing the non-local integral on the current configuration using an updated element interaction matrix instead of a fixed one for all but infinitesimal deformations. The updated non-local GTN model is capable of capturing a more realistic crack propagation which converges with mesh refinement, whereas the local GTN model only gives reliable results of the crack initiation. Several authors report problems with overly aggressive delocalization of the damage parameter, and proposals have been made to regularize the damage parameter indirectly, e.g., Enakoutsa (2014) proposed to average the logarithm of the damage parameter instead. As an alternative, the problem of excessive smoothing could be resolved by evaluating the non-local integral over the current configuration, i.e., by constantly updating the element interaction matrix resulting from the discretization of the integral. With finite strains, the distances between elements change notably, and at fracture often significantly. By neglecting this change in interelement distance and still using the initial interaction values between elements, the smoothing will necessarily be overly aggressive as demonstrated herein.

4 Conclusions

A non-local GTN model on integral form has been implemented as a user-material model for the explicit solver of the FE software Abaqus and applied to model damage evolution and crack propagation in material test specimens until complete fracture. We adopted a modified version of a damage delocalization model proposed by Leblond et al. (1994) and applied by Tvergaard & Needleman (1995). By changing the incremental update of the non-local damage variable, in this case the porosity, adopting essentially a staggered approach, the non-local GTN model gave mesh-independent results for the global response, width of the localization band, and crack initiation and propagation, provided

the non-local integral was evaluated on the current configuration so that the element interaction matrix was continuously updated. Problems discussed in the literature with over-aggressive regularization are seemingly solved by evaluating the non-local integral on the current configuration. A non-local simulation storing the element interaction matrix from the initial configuration is only valid for infinitesimal strains, and continuing use of initial distances between integration points will result in varying degrees of over-aggressive regularization for finite-strain problems. The only difference between the local and non-local GTN models is the introduction of a material characteristic length through a non-local integral which removes the mesh dependency. As demonstrated herein, this retains the applicability of the GTN model while solving a major problem in the modelling of crack initiation and propagation.

Acknowledgements

The present work has been carried out with financial support from Centre of Advanced Structural Analysis (CASA), Centre for Research-based Innovation, at the Norwegian University of Science and Technology (NTNU) and the Research Council of Norway through project no. 237885 (CASA).

References

Andrade, F. X. C., Cesar de Sa, J. M. A., & Andrade Pires, F. M. (2014). Assessment and comparison of non-local integral models for ductile damage. *International Journal of Damage Mechanics, 23*, 261-296. doi:https://doi.org/10.1177/1056789513493103

Andrade, F. X. C., César de Sá, J. M. A., & Andrade Pires, F. M. (2011). A Ductile Damage Nonlocal Model of Integral-type at Finite Strains: Formulation and Numerical Issues. *International Journal of Damage Mechanics, 20*(4), 515-557. doi:https://doi.org/10.1177/1056789510386850

Aravas, N. (1987). On the numerical integration of a class of pressure-dependent plasticity models. *International Journal for Numerical Methods in Engineering, 24*(7), 1395-1416. doi:https://doi.org/10.1002/nme.1620240713

Bahrami Ghalehjoogh, H., & Hoseini, S. H. (2018). Ductile Fracture Analysis of High-strength Steel Bars Using Micromechanical GTN Model. *Journal of Stress Analysis, 2*(2), 31-42. doi:https://doi.org/10.22084/jrstan.2018.15463.1039

Bazant, Z., & Lin, F. B. (1988). Non-local yield limit degradation. *International Journal for Numerical Methods in Engineering, 26*, 1805-1823. doi:https://doi.org/10.1002/nme.1620260809

Belnoue, J. P., Garnham, B., Bache, M., & Korsunsky, A. M. (2010). The use of coupled nonlocal damage-plasticity to predict crack growth in ductile metal plates. *Engineering Fracture Mechanics, 77*(11), 1721-1729. doi:https://doi.org/10.1016/j.engfracmech.2010.03.001

Benzerga, A. A., Besson, J., & Pineau, A. (2004). Anisotropic ductile fracture: Part II: theory. *Acta Materialia, 52*(15), 4639-4650. doi:https://doi.org/10.1016/j.actamat.2004.06.019

Benzerga, A. A., & Leblond, J. B. (2010). Ductile Fracture by Void Growth to Coalescence. *Advances in Applied Mechanics, 44*, 169-305. doi:https://doi.org/10.1016/S0065-2156(10)44003-X

Chu, C., & Needleman, A. (1980). Void Nucleation Effects in Biaxially Stretched Sheets. *Journal of Engineering Materials and Technology, 102*, 249. doi:https://doi.org/10.1115/1.3224807

Dæhli, L. E., Morin, D., Børvik, T., & Hopperstad, O. S. (2017). A Lode-dependent Gurson model motivated by unit cell analyses. *Engineering Fracture Mechanics, 190*. doi:https://doi.org/10.1016/j.engfracmech.2017.12.023

Enakoutsa, K. (2014). An improved nonlocal Gurson model for plastic porous solids, with an application to the simulation of ductile rupture tests. *Applied Mathematical Modelling, 38*(11), 2791-2799. doi:https://doi.org/10.1016/j.apm.2013.11.007

Enakoutsa, K., Leblond, J. B., & Perrin, G. (2007). Numerical implementation and assessment of a phenomenological nonlocal model of ductile rupture. *Computer Methods in Applied Mechanics and Engineering, 196*(13), 1946-1957. doi:https://doi.org/10.1016/j.cma.2006.10.003

Engelen, R. A. B., Geers, M. G. D., & Baaijens, F. P. T. (2003). Nonlocal implicit gradient-enhanced elasto-plasticity for the modelling of softening behaviour. *International Journal of Plasticity, 19*(4), 403-433. doi:https://doi.org/10.1016/S0749-6419(01)00042-0

Geers, M. G. D., de Borst, R., Brekelmans, W. A. M., & Peerlings, R. H. J. (1998). Strain-based transient-gradient damage model for failure analyses. *Computer Methods in Applied Mechanics and Engineering, 160*(1), 133-153. doi:https://doi.org/10.1016/S0045-7825(98)80011-X

Gholipour, H., Biglari, F. R., & Nikbin, K. (2019). Experimental and numerical investigation of ductile fracture using GTN damage model on in-situ tensile tests. *International Journal of Mechanical Sciences, 164*, 105170. doi:https://doi.org/10.1016/j.ijmecsci.2019.105170

Gologanu, M., Leblond, J. B., & Devaux, J. (1993). Approximate models for ductile metals containing non-spherical voids—Case of axisymmetric prolate ellipsoidal cavities. *Journal of the Mechanics and Physics of Solids, 41*(11), 1723-1754. doi:https://doi.org/10.1016/0022-5096(93)90029-F

Gurson, A. L. (1977). Continuum Theory of Ductile Rupture by Void Nucleation and Growth: Part I—Yield Criteria and Flow Rules for Porous Ductile Media. *Journal of Engineering Materials and Technology, 99*(1), 2-15. doi:https://doi.org/10.1115/1.3443401

Hakansson, P., Wallin, M., & Ristinmaa, M. (2006). Thermomechanical response of non-local porous material. *International Journal of Plasticity, 22*, 2066-2090. doi:https://doi.org/10.1016/j.ijplas.2005.08.003

Hütter, G., Linse, T., Mühlich, U., & Kuna, M. (2013). Simulation of ductile crack initiation and propagation by means of a non-local Gurson-model. *International Journal of Solids and Structures, 50*(5), 662-671. doi:https://doi.org/10.1016/j.ijsolstr.2012.10.031

Imran, M., & Bambach, M. (2018). Towards the damage evaluation using Gurson-Tvergaard-Needleman (GTN) model for hot forming processes. *AIP Conference Proceedings, 1960*(1), 170006. doi:https://doi.org/10.1063/1.5035063

Jiang, W., Li, Y., & Su, J. (2016). Modified GTN model for a broad range of stress states and application to ductile fracture. *European Journal of Mechanics - A/Solids, 57*, 132-148. doi:https://doi.org/10.1016/j.euromechsol.2015.12.009

Keralavarma, S. M., & Benzerga, A. A. (2010). A constitutive model for plastically anisotropic solids with non-spherical voids. *Journal of the Mechanics and Physics of Solids, 58*(6), 874-901. doi:https://doi.org/10.1016/j.jmps.2010.03.007

Leblond, J. B., Perrin, G., & Devaux, J. (1994). Bifurcation Effects in Ductile Metals With Nonlocal Damage. *Journal of Applied Mechanics, 61*, 236. Retrieved from https://ui.adsabs.harvard.edu/abs/1994JAM....61..236L

Linse, T., Hütter, G., & Kuna, M. (2012). Simulation of crack propagation using a gradient-enriched ductile damage model based on dilatational strain. *Engineering Fracture Mechanics, 95*, 13-28. doi:https://doi.org/10.1016/j.engfracmech.2012.07.004

Nahshon, K., & Hutchinson, J. W. (2008). Modification of the Gurson Model for shear failure. *European Journal of Mechanics - A/Solids, 27*(1), 1-17. doi:https://doi.org/10.1016/j.euromechsol.2007.08.002

Needleman, A. (1988). Material rate dependence and mesh sensitivity in localization problems. *Computer Methods in Applied Mechanics and Engineering, 67*(1), 69-85. doi:https://doi.org/10.1016/0045-7825(88)90069-2

Needleman, A., & Tvergaard, V. (1984). An analysis of ductile rupture in notched bars. *Journal of the Mechanics and Physics of Solids, 32*(6), 461-490. doi:https://doi.org/10.1016/0022-5096(84)90031-0

Needleman, A., & Tvergaard, V. (1998). Dynamic crack growth in a nonlocal progressively cavitating solid. *European Journal of Mechanics - A/Solids, 17*(3), 421-438. doi:https://doi.org/10.1016/S0997-7538(98)80053-3

Nguyen, G., Korsunsky, A., & Belnoue, J. (2014). A nonlocal coupled damage-plasticity model for the analysis of ductile failure. *International Journal of Plasticity, 64*. doi:https://doi.org/10.1016/j.ijplas.2014.08.001

Oh, Y. R., Nam, H. S., Kim, Y. J., & Miura, N. (2017). Simulation of ductile crack growth in cracked pipes using the gtn model. Retrieved from http://www.lib.ncsu.edu/resolver/1840.20/35909

Pardoen, T., & Hutchinson, J. W. (2000). An extended model for void growth and coalescence. *Journal of the Mechanics and Physics of Solids, 48*(12), 2467-2512. doi:https://doi.org/10.1016/S0022-5096(00)00019-3

Peerlings, R. H. J., de Borst, R., Brekelmans, W. A. M., & Geers, M. G. D. (2002). Localisation issues in local and nonlocal continuum approaches to fracture. *European Journal of Mechanics - A/Solids, 21*(2), 175-189. doi:https://doi.org/10.1016/S0997-7538(02)01211-1

Peerlings, R. H. J., Poh, L. H., & Geers, M. G. D. (2012). An implicit gradient plasticity–damage theory for predicting size effects in hardening and softening. *Engineering Fracture Mechanics, 95*, 2-12. doi:https://doi.org/10.1016/j.engfracmech.2011.12.016

Pineau, A., Benzerga, A. A., & Pardoen, T. (2016). Failure of metals I: Brittle and ductile fracture. *Acta Materialia, 107*, 424-483. doi:https://doi.org/10.1016/j.actamat.2015.12.034

Qiang, B., & Wang, X. (2019). Ductile crack growth behaviors at different locations of a weld joint for an X80 pipeline steel: A numerical investigation using GTN models. *Engineering Fracture Mechanics, 213*, 264-279. doi:https://doi.org/10.1016/j.engfracmech.2019.04.009

Ramaswamy, S., & Aravas, N. (1998). Finite element implementation of gradient plasticity models Part II: Gradient-dependent evolution equations. *Computer Methods in Applied Mechanics and Engineering, 163*(1), 33-53. doi:https://doi.org/10.1016/S0045-7825(98)00027-9

Reusch, F., Hortig, C., & Svendsen, B. (2008). Nonlocal Modeling and Simulation of Ductile Damage and Failure in Metal Matrix Composites. *Journal of Engineering Materials and Technology, 130*, 021009. doi:https://doi.org/10.1115/1.2840967

Reusch, F., Svendsen, B., & Klingbeil, D. (2003). Local and non-local Gurson-based ductile damage and failure modelling at large deformation. *European Journal of Mechanics - A/Solids, 22*(6), 779-792. doi:https://doi.org/10.1016/S0997-7538(03)00070-6

Samal, M. K., Seidenfuss, M., Roos, E., Dutta, B. K., & Kushwaha, H. S. (2008). Finite element formulation of a new nonlocal damage model. *Finite Elements in Analysis and Design, 44*(6), 358-371. doi:https://doi.org/10.1016/j.finel.2007.12.002

Seabra, M. R. R., Šuštarič, P., Cesar de Sa, J. M. A., & Rodič, T. (2013). Damage driven crack initiation and propagation in ductile metals using XFEM. *Computational Mechanics, 52*(1), 161-179. doi:https://doi.org/10.1007/s00466-012-0804-9

Seidenfuss, M., Samal, M. K., & Roos, E. (2011). On critical assessment of the use of local and nonlocal damage models for prediction of ductile crack growth and crack path in various loading and boundary conditions. *International Journal of Solids and Structures, 48*(24), 3365-3381. doi:https://doi.org/10.1016/j.ijsolstr.2011.08.006

Seupel, A., Hütter, G., & Kuna, M. (2018). An efficient FE-implementation of implicit gradient-enhanced damage models to simulate ductile failure. *Engineering Fracture Mechanics, 199*, 41-60. doi:https://doi.org/10.1016/j.engfracmech.2018.01.022

Simone, A., Wells, G. N., & Sluys, L. J. (2003). From continuous to discontinuous failure in a gradient-enhanced continuum damage model. *Computer Methods in Applied Mechanics and Engineering, 192*(41), 4581-4607. doi:https://doi.org/10.1016/S0045-7825(03)00428-6

Teng, B., Wang, W., & Xu, Y. (2017). Ductile fracture prediction in aluminium alloy 5A06 sheet forming based on GTN damage model. *Engineering Fracture Mechanics, 186*, 242-254. doi:https://doi.org/10.1016/j.engfracmech.2017.10.014

Tvergaard, V. (1981). Influence of voids on shear band instabilities under plane strain conditions. *International Journal of Fracture, 17*(4), 389-407. doi:https://doi.org/10.1007/BF00036191

Tvergaard, V. (1982). On localization in ductile materials containing spherical voids. *International Journal of Fracture, 18*(4), 237-252. doi:https://doi.org/10.1007/BF00015686

Tvergaard, V., & Needleman, A. (1984). Analysis of the cup-cone fracture in a round tensile bar. *Acta Metallurgica, 32*(1), 157-169. doi:https://doi.org/10.1016/0001-6160(84)90213-X

Tvergaard, V., & Needleman, A. (1995). Effects of nonlocal damage in porous plastic solids. *International Journal of Solids and Structures, 32*(8), 1063-1077. doi:https://doi.org/10.1016/0020-7683(94)00185-Y

Tvergaard, V., & Needleman, A. (1997). Nonlocal effects on localization in a void-sheet. *International Journal of Solids and Structures, 34*(18), 2221-2238. doi:https://doi.org/10.1016/S0020-7683(96)00140-0

Zybell, L., Hütter, G., Linse, T., Mühlich, U., & Kuna, M. (2014). Size effects in ductile failure of porous materials containing two populations of voids. *European Journal of Mechanics - A/Solids, 45*, 8-19. doi:https://doi.org/10.1016/j.euromechsol.2013.11.006